



Unveiling the synergistic effects of pH and Sn content for tuning the catalytic performance of Ni⁰/Ni_xSn_y intermetallic compounds dispersed on Ce-Zr mixed oxides in the aqueous phase reforming of ethylene glycol

Consolato Rosmini^{a,*}, Monica Pazos Urrea^b, Enrico Tusini^c, Sylvio Indris^d, Daniela Kovacheva^e, Daniela Karashanova^f, Hristo Kolev^g, Anna Zimina^{c,h}, Jan-Dierk Grunwaldt^{c,h}, Magnus Rønning^b, Momtchil Dimitrov^a, Margarita Popova^{a,*}

^a Institute of Organic Chemistry with Centre of Phytochemistry, Bulgarian Academy of Sciences, Acad. G. Bonchev str, bl. 9, Sofia 1113, Bulgaria

^b Department of Chemical Engineering, Norwegian University of Science and Technology, Trondheim 7491, Norway

^c Institute for Chemical Technology and Polymer Chemistry, Karlsruhe Institute of Technology, Engesserstraße 20, Karlsruhe 76131, Germany

^d Institute for Applied Materials-Energy Storage Systems (IAM-ESS), Karlsruhe Institute of Technology (KIT), Hermann-von-Helmholtz-Platz 1, Eggenstein-Leopoldshafen 76344, Germany

^e Institute of General and Inorganic Chemistry, Bulgarian Academy of Sciences, Acad. G. Bonchev Str, bl. 11, Sofia 1113, Bulgaria

^f Institute of Optical Materials and Technologies, Bulgarian Academy of Sciences, Acad. G. Bonchev Str, bl. 109, Sofia 1113, Bulgaria

^g Institute of Catalysis, Bulgarian Academy of Sciences, Acad. G. Bonchev Street, bl. 11, Sofia 1113, Bulgaria

^h Institute of Catalysis Research and Technology, Karlsruhe Institute of Technology, Hermann-von-Helmholtz Platz 1, Eggenstein-Leopoldshafen 76344, Germany

ARTICLE INFO

Keywords:

Ethylene Glycol aqueous phase reforming
Ni-Sn intermetallic compounds
Initial alkaline pH
Induced Cannizzaro reaction
H₂ and glycolic acid production

ABSTRACT

The product distribution in aqueous phase reforming (APR) of polyols is closely tied to the catalytically induced feed cleavage mechanism. Strategic variations in catalyst composition and synergistic effects prompted by reaction conditions, such as pH, can be utilized to tune the product distribution of both liquid and gaseous phases. This study aimed to compare the physicochemical properties of various Ni_xSn_y/Ce(Zr)O₂ catalysts and their performance in batch tests during the APR of a 6%wt. ethylene glycol (EG) solution under both neutral and alkaline conditions. The results show that the progressive addition of tin strongly tunes the activity of the catalysts and the nickel-induced methanation reaction under neutral conditions, albeit decreasing feed conversions. In synergy with tin tuning, the alkaline environment boosts the process by increasing conversions and H₂-yields while still minimizing methanation due to the alkali-induced process of Cannizzaro disproportionation of EG into glycolic acid with subsequent reforming thereof.

1. Introduction

In recent years, the energy and climate crises, both linked to the massive consumption of fossil fuels, have led research towards the development of processes that can at least partially supplant the demand of petrol derivatives. The hydrogen molecule has been identified as one of the most suitable energy carriers for this purpose, due to its high gravimetric energy density (120–142 MJ/kg, compared to 44.5 MJ/kg for gasoline) [1], a quality which, in combination with the most advanced fuel cell developments, would lead to the clean emission of water [2] (2H₂ + O₂ → 2H₂O; ΔE = −286 kJ/mole). At present, more than 96% of hydrogen production is interdependent on fossil fuels and

only a small niche market is devoted to what is called low emission hydrogen according to the report released in 2022 by the International Energy Agency (IEA). One of the synthetic strategies to favor hydrogen production with a lower economic and environmental impact would be the use of biomass as a substitute for fossil derivatives. The integration of multiple processes to obtain goods of different nature from biomass falls within the biorefinery definition. Specifically, efforts have been made in bio-diesel production using this technology concept. However, it has been observed that the bio-diesel production processes currently in use have the disadvantage that full utilization of the starting biomass is not achieved. It has been estimated that the bio-diesel industry produces 1 kg of raw glycerol as waste for every 10 kg of finished product [3].

* Corresponding authors.

E-mail addresses: consolato.rosmini@orgchm.bas.bg (C. Rosmini), margarita.popova@orgchm.bas.bg (M. Popova).

<https://doi.org/10.1016/j.apcatb.2024.123904>

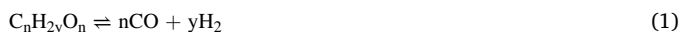
Received 14 December 2023; Received in revised form 15 February 2024; Accepted 29 February 2024

Available online 2 March 2024

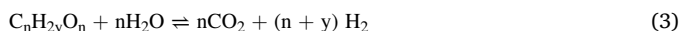
0926-3373/© 2024 The Authors. Published by Elsevier B.V. This is an open access article under the CC BY-NC-ND license (<http://creativecommons.org/licenses/by-nc-nd/4.0/>).

Glycerol is not the only polyol to be produced in large, if not harmful quantities by the industry. Ethylene glycol is a raw material widely used in production processes in textiles, leather, rubber, and chemical fibers, and is often found as a waste material in industrial aqueous residues [4]. The method for further reuse of industrially produced polyols can be found in the conversion of these molecules into hydrogen and carbon dioxide by reforming processes. Furthermore, being the simplest of polyols, its use as a model for a rational approach dedicated to understanding the cleavage pathways occurring in the mentioned processes is certainly advantageous.

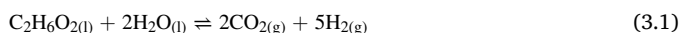
Aqueous phase reforming (APR) is a process first reported in 2002 by Cortright and co-workers, with the aim of exploiting short-chain oxygenated molecules, in aqueous phase, to produce gaseous mixtures with high hydrogen content [5]. The advantages of this process are multiple. Working at pressures between 20 and 60 bar, at low temperatures (220–270 °C), it avoids vaporization of the aqueous mixture, lowering reforming temperatures in comparison with conventional steam reforming processes operating at temperatures between 700 and 800 °C [5]. It was also reported by Davda et al. [6] that the use of oxygenated hydrocarbons at the above-mentioned conditions promotes hydrogen formation at lower temperatures than the use of saturated hydrocarbons. The reaction stoichiometry is reported in equation (Eq. 1):



The studies by Davda et al. [5,6] also clarified the preponderant role during APR of oxygenated hydrocarbons for the *water-gas shift reaction* (WGS; Eq. 2), which is highly favored at mild operating temperatures, leading to a gaseous mixture containing a negligible amount of CO. Combining Eqs. (1) and (2), one can deduce the conventional reaction stoichiometry for APR (Eq. 3).



For a target molecule such as ethylene glycol, the following equation (Eq. 3.1) will then be obtained:



However, the operating conditions for aqueous phase reforming present certain drawbacks. The production of H₂ and CO₂ at low temperatures has selectivity limitations, since under the same conditions the reaction to form alkanes from the reaction products H₂, CO₂ and CO become highly competitive, an exemplary reaction described by Eq. 4 is the CO₂ methanation reaction.



An efficient catalyst to produce hydrogen from aqueous phase reforming of oxygenated hydrocarbons must facilitate hydrogen-producing processes such as the water-gas shift reaction. The selectivity of the catalyst in the feed cleavage mechanism thus is crucial to the final products of the reaction [6]. As far as ethylene glycol is concerned, the cleavage of the C-C single bond is what is recognized as the hydrogen-productive mechanism in APR. Cleavage of the C-O bond, on the other hand, would favor rearrangements and tautomerization of the derived molecules, which would favor hydrogen-consuming reactions with the formation of long-chain alcohols and polyols (C₃₋₄-(OH)_x), in turn reformed into short and long chain alkanes or formation of carboxylic acids [7]. Many metals, bimetallic combinations and catalytic supports have been investigated to find a good compromise between catalytic activity and selectivity for hydrogen production at the expense of alkane-producing reactions. Platinum is the most studied active metal in APR, as it combines high activity coupled with moderate selectivity [6,8]. Nickel also has a high conversion of the organic feed, but according to numerous studies it has also a high selectivity to the

methanation reaction (Eq. 4) [8]. The high content of CH₄, CO₂ and traces of CO usually obtained from Ni-based catalysts could make the gas mixture produced less attractive from a practical point of view during the hydrogen purification step for commercial purposes than a mixture consisting mainly of H₂ and CO₂. In fact, the process currently used for such separation is pressure swing adsorption (PSA), a continuous multi-step process with considerable system and energy costs [9]. This process involves a preliminary CO₂ capture step followed by the actual PSA in which the hydrogen is separated from the other products, generally considered as waste. However, there are also other process types such as Gemini [10] and VPSA [9] that are capable of co-separating and storing in a single absorption cycle H₂ and CO₂ with high purities, valorizing both products.

It has already been demonstrated by Huber et al. [11], that the addition of tin to a Raney-Ni catalyst (Raney®-Ni 2800 -Grace-Davison, Ni content >89%) significantly decreases, in neutral environment, the selectivity for the methanation reaction while maintaining the hydrogen production. This is effectively demonstrating how Ni_xSn_y intermetallic compounds (IMCs) can be used to modulate the selectivity to the reaction products. Additionally, the choice of catalytic support as well as that of the initial pH value of the reaction medium [6,12,13] also seem to influence the cleavage mechanisms of the feed on the catalyst surface by increasing its conversion but making the rationalization of the obtained products in the gaseous and liquid phase more complex and often poorly clarified. This study aims to combine the aforementioned findings, investigating the catalytic behavior brought by the combination of different assets of Sn, Ni and Ni_xSn_y IMCs dispersed on Ce(Zr)O₂ mixed oxides in the aqueous phase reforming of ethylene glycol (6 wt%) under neutral or alkaline batch conditions. The objective of a rational study of the liquid and gaseous phase products observed using the mono- or bimetallic catalysts, is to display the fundamental role of tin in interaction with nickel as a tuning agent for the choice of competitive hydrogen-producing cleavage pathways, synergistically with initial pH-induced benefits.

2. Experimental

2.1. Materials

The catalyst support Ce(Zr)O₂, was synthesized by micellar-assisted hydrothermal synthesis with a procedure like the one detailed by Tsoncheva et al. [14]. In this regard, a 0.3 M aqueous solution of hexadecyltrimethylammonium bromide (CTAB) was prepared and left to stand under magnetic stirring until complete solubilization of the micellar reagent. Separately, the CeCl₃·7H₂O and ZrCl₄ salts, have been used as precursors for the mixed metal oxides of cerium and zirconium, after being solubilized in water with a molar ratio Ce/Zr = 2. Subsequently, the aqueous solution containing the metal precursors was added under magnetic stirring to that containing the micellar agent. An aqueous solution of NH₄OH at 12.5% was added dropwise to reach a pH of about 10, to allow precipitation of the metal hydroxides in the solution. The emulsion was kept under magnetic stirring at 50 °C per 10 hours. The hydrothermal treatment was carried out in a Teflon lined autoclave at 100 °C for 24 h. The solid obtained after the washing and drying process at room temperature was calcined in a muffle furnace under static atmosphere for 10 hours at 300 °C.

The loading of the cerium-zirconium mixed metal oxides with tin oxide and/or nickel oxide was achieved by incipient wetness impregnation of 2 g portions of support (CZ support) with a theoretical amount equal to 10 wt% of Ni using Ni(NO₃)₂·6H₂O as precursor (“oxidized monometallic catalyst” designated 10Ni-CZ). A similar approach was used for the loading of the CZ-support with 2.5, 5 and 10 wt% of Sn, using SnCl₂·2H₂O as precursor (“oxidized monometallic catalysts” designated 2.5Sn-CZ, 5Sn-CZ, and 10Sn-CZ, respectively). The incipient wetness co-impregnation of the combination of different theoretic amounts of tin with 10 wt% nickel, were instead used to produce the

oxidized bimetallic catalysts reported in the present work as 2.510SnNi-CZ, 510SnNi-CZ, and 1010SnNi-CZ.

The process of reduction and formation of the metallic and inter-metallic compounds of $\text{Ni}^0/\text{Ni}_3\text{Sn}_7$ actively used in APR was obtained by reductive treatment in an environment containing pure hydrogen (purity 5.0) with a flow rate of 50 mL/min during a temperature ramp from 50 to 550 °C at 10 °C/min and an isothermal period at 550 °C for 4 hours. Following the reduction process, the reactor was cooled down to room temperature for catalyst passivation (100 mL 1% O_2/Ar for 1 hour), before proceeding of the catalytic test. All the samples obtained from the reduction and passivation process are designated in the present work by adding the suffix "_red" to the previously defined names.

2.2. Characterization methods

LA-ICP-MS system was used to analyze the Sn and Ni content in the samples, the instrumentation consists of NewWave UP193FX laser and PerkinElmer Elan DRC-e ICP-MS. For controlled ablation of the samples, an energy density of around 5 J/cm² on the sample surface and a laser pulse frequency of 4–6 Hz were used. Analyses were generally performed with 35–50 μm beam diameters. External standardization on the NIST SRM-610/617 glass standard provides relative elemental concentrations. These relative concentrations were transformed into wt% by using the Zr and Ce content in the support as an internal standard, determined by XRF.

Low-temperature N_2 physisorption isotherms were obtained by a Quantachrome Instruments AUTOSORB iQ-C-MP-AG-AG NOVA 1200e (USA) apparatus. The specific surface area was determined from the Brunauer Emmett Teller (BET) equation, the total pore volume (V_{tot}) was obtained at a relative pressure of 0.99 p/p_0 using the BJH method. The same method was applied to the desorption branch of the isotherms to obtain the average pore diameter (D_{pores}) and the pore size distribution.

Powder X-ray diffraction patterns were collected on a Bruker D8 Advance diffractometer with $\text{Cu K}\alpha$ radiation and a LynxEye detector with constant step of 0.02° 2 θ and counting time of 17.5 s per step. DiffraPlus EVA 2 and ICDD-PDF2 (2014) database were used for phase composition identification. Unit cell parameters and mean crystallite sizes were determined by Rietveld refinement using Topas-4.2 software [15]. Further information on the data analysis has been reported in paragraph 3 of the [supporting information](#).

¹¹⁹Sn Mössbauer experiments were performed at room temperature in transmission geometry and in constant-acceleration mode with a CaSnO_3 source. The velocity scale was calibrated with $\beta\text{-Sn}$ metal foil and all isomer shifts are given relative to that of BaSnO_3 .

The samples for TEM investigations were finely dispersed in a hydroalcoholic solution (ethanol / water = 2), dropped onto Cu TEM grids, and dried in an uncontaminated environment. TEM analysis was performed by means of JEOL JEM 2100 high resolution transmission electron microscope at accelerating voltage of 200 kV. Selected area electron diffraction (SAED) mode was applied for diffraction patterns accumulation and HR-TEM imaging was used for lattice fringes registration.

H_2 chemisorption experiments were carried out in a Quantachrome Instruments AUTOSORB iQ-C-MP-AG-AG NOVA 1200e apparatus. 700 mg of calcined material were loaded into a U-shaped quartz reactor and placed between quartz wool plugs. The catalyst was reduced *in situ* under a flow of 50 mL/min of pure hydrogen from room temperature to 550 °C at a heating rate of 10 °C/min and a reduction isotherm at 550 °C for 4 hours. After reduction, the sample was treated in helium (flow 50 mL/min) for 30 min at 550 °C. Afterwards, the material was cooled down to 40 °C, and evacuation took place for 30 min. The exposed active metal surface was calculated based on H_2 uptake. A H/Ni adsorption stoichiometric factor of 1 was used [7].

The oxidized monometallic and bimetallic samples were subjected to a thermogravimetric analysis in programmed temperature reduction

(TPR-TGA), in a Netzsch STA 449-F5 Jupiter thermogravimetric microbalance. For this purpose, 50 mg of all samples were pre-treated in an inert atmosphere (pure N_2 N60; flow 50 mL/min) in an isotherm of 200 °C for 40 minutes, to eliminate moisture or contaminants. Only after having lowered the temperature up to 30 °C in an inert environment, 50 mL/min of H_2 (5% in Ar for safety reasons dictated by the apparatus) was flushed during a temperature-programmed ramp at 5 °C/min up to 550 °C. Once the temperature of 550 °C was reached, the thermogravimetric analysis continued for 4 hours.

Ex-situ X-ray absorption spectroscopy (XAS) was performed at the CAT-ACT beamline at the KIT Light Source [16]. The catalysts were diluted in a ratio of 1:4 with cellulose to mitigate the high absorption deriving from the large quantities of cerium and zirconium of the catalytic support, and subsequently pelletized. The x-ray absorption was measured in transmission with Ni foil as reference behind the sample; The inflection point (major maximum of the first derivative) of the tabulated value of 8333 keV for the Ni K-edge of Ni-foil was used for the energy calibration. The XANES spectra were calibrated and edge step normalized in accordance with the standard procedure of data reduction [17], using the Athena package. The normalization procedure involved linear regression fitting in the pre-edge region (-150 to -30 eV) and a third-order polynomial function in the post-edge region (35–727 eV). The EXAFS signals $\chi(k)$ were extracted and then Fourier-transformed by mean of a Kaiser-Bessel window ranging from 3 to 12 Å⁻¹ using the Artemis package of Demeter IFEFFIT software [18]. FEFF6 was used to obtain phase shift and amplitude considering a metallic cluster of Nickel atoms and Ni-O and Ni-Sn scattering path at the Ni K-edge [19], utilizing the Crystallographic Information Files obtained from the X-ray diffraction analysis of the samples. All data were k-weighted to the third power and just single scattering events were considered during the fitting procedure of the first coordination shell. The S_0^2 value was fixed at 0.84 (Ni as an adsorbing atom) obtained by the fitting of Ni standard. The fitting of the R-space was kept within the radial distance window of 1–3 Å referred to a reciprocal k-space of the data with $\Delta k = 8.0 \text{ Å}^{-1}$. The representation of the Fourier transform in the reciprocal space (Q), incorporates the wavenumber (k)-window from 3 to 12 Å⁻¹.

Ex-situ X-ray photoelectron measurements have been carried out on the ESCALAB MkII (VG Scientific, now Thermo Scientific) electron spectrometer with a base pressure in the analysis chamber of 5×10^{-10} mbar (9×10^{-9} mbar during the measurements), equipped with twin anode $\text{MgK}\alpha/\text{AlK}\alpha$ non-monochromated X-ray source that used excitation energies of 1253.6 and 1486.6 eV, respectively. The measurements are provided only with $\text{AlK}\alpha$ non-monochromated X-ray source (1486.6 eV). The pass energy of the hemispherical analyzer was 20 eV was used. The instrumental resolution measured as the full width at a half maximum (FWHM) of the Ag3d5/2 , photoelectron peak is about 1 eV. The energy scale has been calibrated by normalizing the C1s line of adventitious hydrocarbons to 285.0 eV for electrostatic sample charging. The data was analyzed by SpecsLab2 CasaXPS software (Casa Software Ltd). The processing of the measured spectra includes a subtraction of X-ray satellites [20] and Shirley-type background [21]. The peak positions and areas are evaluated by a symmetrical Gaussian-Lorentzian (50% Lorentzian contribution) curve fitting. The relative concentrations of the different chemical species are determined based on normalization of the peak areas to their photoionization cross-sections, calculated by Scofield [22]. The multiplet splittings and area ratios were constrained according to the parameters indexed in [23] of the core level related to the species. The absolute binding energy values and FWHM were allowed to vary by $\pm 0.1\text{--}0.2$ eV respectively to allow a better self-adjustment for error associated with charge referencing to adventitious C 1 s.

2.3. Catalytic tests

Aqueous phase reforming reactions were performed in a stainless-steel bench reactor (Parr 4848) using the setup reported in a previous

study by Pazos Urrea et al. [24]. 0.5 g of pre-reduced catalyst (as in Section 2.2) was transferred into the reactor containing 6 wt% ethylene glycol (EG-6%) solution. The reactor was purged with nitrogen flow and pressurized with an initial pressure of 20 bar which served also as internal standard for the quantification of the gaseous products. The reactor was then heated at 270 °C and held at this temperature for 2 h. Finally, the reactor was cooled down by means of an ice bath to room temperature. The gaseous products were collected in a sampling gas bag and analyzed with a GC (Agilent 7820 A equipped with thermal conductivity detector (TCD) flame ionization detector (FID) and Porapak-Q GS-Q, CP-Molsieve 5 Å and HP-Plot Al₂O₃ KCl columns. After depressurization, the liquid products were collected and filtered with a 0.25 µm PTFE filter and analyzed with a HPLC 1260 Infinity II LC System Agilent technologies with a refractive index detector. The products were separated using an Agilent Hi-Plex H ion exclusion column 300 mm×7.7 mm with a mobile phase of 5 mM sulfuric acid, with a flow rate of 0.6 mL/min and a temperature of 60 °C. The presence of the various products in the liquid phase has been confirmed by GC-MS (Agilent 7820 A GC coupled with an Agilent 5975 MSD fitted with a VF-Xms fused silica column 70 m × 250 µm × 1 µm. For all sample analysis, the GC-MS oven was programmed from 40 °C, held for 1 min, then increased from 40 °C to 270 °C at 10 °C/min and held for 20 min (helium was used as carrier gas). As known from the studies of van Haasterecht et al. [13], the initial pH values of the EG solution decrease dramatically during the APR in batch conditions, due to the formation of carboxylic acids and other protic molecules. Knowing the above, two different conditions of initial pH values were investigated in the present study and for practical simplicity nomenclated: neutral and alkaline conditions. At neutral conditions 30 mL of EG-6% was used together with 0.5 g of reduced catalyst, with an initial value of pH_i = 7. The reaction under alkaline conditions takes place with the addition of 0.6 g of KOH tablets dissolved in the 30 mL of EG-6%, with an initial value of pH_i = 14. The equations applied to evaluate the catalyst performance during aqueous phase reforming in batch conditions are shown in Table S0.

3. Results and discussion

3.1. Phase composition, textural and morphological characterization

N₂ physisorption measurements were carried out for all synthesized samples and the adsorption-desorption isotherms are shown in Figure S1. The shape of the isotherms of the samples can be classified as of type IVa, with a hysteresis between values 0.4 and 0.85 p/p₀, due to a pore width greater than 2 nm, classifying all reported materials as primarily mesoporous [25]. The portion of the hysteresis loop positioned at partial pressures higher than 0.9 p/p₀ can be attributed to larger mesopores and interparticle macroporosity. The CZ support exhibits an apparent H3-type hysteresis loop (Figure S1), having a lower limit of the desorption branch at the cavitation-induced p/p₀ generally associated with slit-shaped pores smaller than 4 nm (Figure S2). The 2.510SnNi-CZ_{based}, 1010SnNi-CZ_{based} and the monometallic catalysts in their oxidized and reduced forms exhibit an H₂-type hysteresis cycle, reflecting a complex and network-dependent pore structure. The increased slope, of the desorption isotherms compared to those of the support, confirm the evolution in pore shape from slit-shaped to ink-bottle pores and an increasing in the pore size (Figure S2, Table 1, D_{pores}) [25,26].

The 510SnNi-CZ_{based} samples, retain a textural structure that can be described as “hybrid” between that represented by an H3 and H2-type hysteresis loop, and a pore size distribution in both samples similar to that of CZ-support (Figure S2, Table 1, D_{pores}). As shown in Table 1, impregnation and subsequent calcination of the CZ-support with nickel and tin salts lead to a significant decrease in the specific surface area (S_{BET}), which may be attributed to a partial congestion of support pores with tin and nickel metal oxide particles. The reduction process of these oxides leads to sintering of occlusions and a slightly higher surface area

Table 1

BET surface area (S_{BET}), total pore volume (V_{tot}) and average pore diameter (D_{pores}) of the specimens in study.

Sample	S _{BET} (m ² /g)	V _{tot} (mL/g)	D _{pores} (nm)
CZ-support	105	0.10	3.6
2.5Sn-CZ	52	0.10	5.2
5Sn-CZ	42	0.08	5.5
10Sn-CZ	45	0.07	6.7
10Ni-CZ	42	0.09	6.2
2.510SnNi-CZ	49	0.11	5.8
510SnNi-CZ	46	0.09	3.5
1010SnNi-CZ	44	0.09	5.5
2.510SnNi-CZ _{red}	51	0.10	5.8
510SnNi-CZ _{red}	57	0.09	3.7
1010SnNi-CZ _{red}	53	0.10	6.2

in the reduced catalysts than in their oxidized counterparts. Analyzing adsorption/desorption isotherms at p/p₀ > 0.95 before and after reduction reveals a substantial decrease in nitrogen desorption volume at high p/p₀ values, indicating a decrease in inter-particle macroporosity attributed to the sintering process.

The XRD pattern of the CZ-support shown in Figure S3-A and described in detail in Section 3 of the supporting information (Figure S3A-B), establishes its composition as being 54.3 wt% of a tetragonal mixed oxide of Ce_{0.5}Zr_{0.5}O₂ (PDF 96–210–2840) and 43.7 wt % from cubic cerianite, with a Ce:Zr atomic ratio of 7:3. The XRD patterns of the monometallic catalysts, in which the CZ support was loaded with 2.5%_{wt.}, 5%_{wt.} and 10%_{wt.} of tin oxide and one with 10%_{wt.} of nickel oxide are shown in Fig. 1-A. In the sample with the lowest tin concentration, no reflections belonging to the stannic oxide were found. Hence, the presence of a low long-range order of the periodic array of the stannic species within the CZ-support can be assumed. The registered distortion of the unit cell parameters of the support mixed oxidized portion, however, could be an effect due to a defective intercalation of Sn⁴⁺ ions within the tetragonal lattice of Ce(Zr)O₂ (Table S1). As the tin concentration increases, there is an evident formation of crystalline tetragonal cassiterite crystallites distinguishable in the diffractogram from the reflections positioned at 2θ = 26.4°, 33.8°, 37.8° and 51.7° (SnO₂, PDF 00–45–1449). The sample 10Ni-CZ shows reflections belonging to the crystallographic planes of cubic bunsenite (NiO, PDF 00–049–1049) located at 2θ = 37.2°, 43.2°.

The reduction of the monometallic catalysts highlights the formation of large metallic domains clearly visible in the XRD pattern of sample 10Sn-CZ_{red} (Fig. 1-B) with the tetragonal tin reflections at 2θ = 30.6°, 31.9°, 43.8° and 44.8° (PDF 01–089–4898). Similarly, the reduction converts the cubic NiO of sample 10Ni-CZ_{red} into Ni⁰, revealed by the characteristic reflections at 2θ = 44.4° and 51.7° (PDF 00–004–085). Figure S4 shows the crystallographic composition of the bimetallic catalysts described in the 2.1 materials section, in both their mixed-metal oxide state (left panel) and post reductive process state (right panel). Similarly to monometallic systems, oxidized bimetallic catalysts exhibit reflections corresponding to cubic NiO (PDF 00–049–1049). The absence of reflections indicative of crystalline cassiterite in these samples, including the catalyst with the highest tin loading (1010SnNi-CZ), suggests that the presence of a nickel phase helps maintain a low long-range order of the periodic array of tin oxide, even at high loadings, compared to monometallic references. This dispersion promotes the formation of Ni_xSn_y IMCs during the reductive treatment (Figure S4, right panel) conferring to the catalysts a different crystallographic arrangements based on the tin content. The 2.510SnNi-CZ_{red} sample at low tin concentrations in fact, shows reflections belonging to Ni⁰ and only a broad peak with low intensity centered at 2θ = 42.3°, cautiously attributable to a Ni₃Sn-type IMC, highly disordered. By increasing the tin concentration (510SnNi-CZ_{red}), the formation of a hexagonal Ni₃Sn phase (PDF-00–035–1362), is highlighted by the appearance of reflections at 2θ = 39.5°, 42.6° and 44.9° belonging to planes (200), (002),

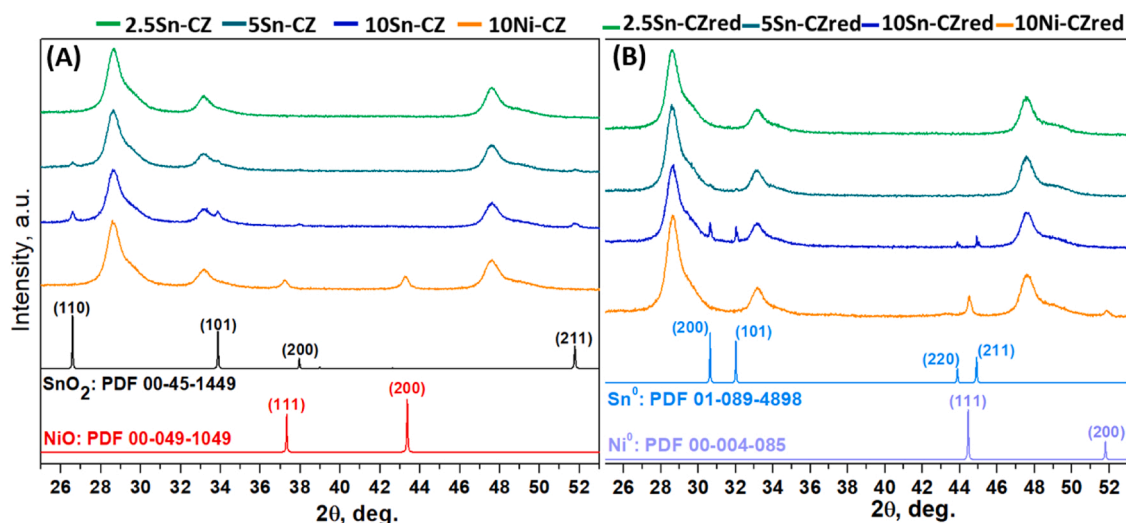


Fig. 1. : Stacked XRD patterns of the oxidized (A) and reduced (B) monometallic Sn and Ni catalysts.

(201) also in this case accompanied by the presence of crystalline Ni^0 particles. The Figure S4-B 2θ region magnification, ranging from 39° to 46° and represented in Fig. 2, not only details what has already been discussed, but sheds light on the complex composition of the sample with the highest tin loading.

In addition to a decreased relative content of metallic nickel, and a presence of crystalline hexagonal Ni_3Sn , sample 1010SnNi-CZ_red exhibits the presence of a high-tin content compound, recognized as Ni_3Sn_2 (PDF 01-072-2561), with an orthorhombic structure. As shown in Fig. 2, to better fit the shape of the observed data of the latter catalyst, it was necessary to model them using two orthorhombic Ni_3Sn_2 IMCs belonging to the $Pnma$ [No. 62] space group with slightly different unit cell parameters (Table S2). A rational explanation for the heterogeneity in cell parameters and crystallite size of Ni_3Sn_2 , as well as the varying crystallinity of Ni_3Sn , can be attributed to the dependence of compound formation on the specific chemical environment encountered by Sn and Ni atoms during sintering in a reductive atmosphere. Support interactions, dispersion and tin loading emerge as critical factors determining the formation of Ni_xSn_y compounds with differing tin content. Evidence supporting this statement can be gleaned from the reduction

profiles of both mono- and bimetallic samples (Figs. S5 and 3). In tin-based monometallic oxidized catalysts, reduction initiates around 162°C , reaching its peak at 296°C for the 2.5Sn-CZ catalyst (Figure S5-A). Catalysts with higher Sn content exhibit a similar onset temperature for reduction but with a broader range extending to higher temperatures. This underscores variations in the interactions between Sn^{4+} ions and the support. Similarly, the reduction profiles of 10Ni-CZ (Fig. 3-A) reveal two distinct reduction processes: The first centered at 345°C , while the second, although less prominent, occurs at a higher temperature of 475°C .

The TPR/TGA analysis of the bimetallic oxidized catalysts (Figs. S5-B and 3-B) reveals a complex reduction process. The initial reduction below 300°C corresponds to the reduction of large NiO and SnO_2 particles. A distinct reduction onset at 318°C marks the beginning of the phase with the highest mass loss rate, occurring between 353 and 364°C for all bimetallic catalysts. The final temperature of this main reduction process increases with the tin oxide concentration, compared to the 10Ni-CZ sample (Fig. 3-B). Additionally, there's a notable decrease in the reduction temperature of the second phase, especially for the 1010SnNi-CZ sample, compared to the monometallic Ni sample. In a similar study by Onda et al. [27] on intermetallic compounds supported on SiO_2 , it's reported that the reduction temperature increases gradually with increasing tin concentration: $\text{Ni} < \text{Ni}_3\text{Sn} < \text{Ni}_3\text{Sn}_2 < \text{Ni}_3\text{Sn}_4$. The reduction profiles of the monometallic tin catalysts (Figure S5-A) exhibit non-linear mass loss behavior, suggesting that cassiterite or Sn^{4+} ions, when well dispersed and strongly retained by the support, require proximity and synergy with bunsenite for efficient reduction; the absence of this interaction leads to only partial reduction of tin in the monometallic catalysts.

To visualize the morphology and nanostructure of the samples, transmission electron microscopy (TEM) was used. Images at different magnification of the selected samples 510SnNi-CZ and 510SnNi-CZ_red are presented in Figure S6 and Fig. 4. The image in Figure S6-A shows the presence of quasi-spherical particles with sizes ranging from 5 to 20 nm in size (Figure S-H). In good agreement with the XRD analysis, Figure S6-B demonstrate in high resolution mode the interplanar distances of the crystallographic planes of CeO_2 , SnO_2 , NiO and $\text{Ce}_x\text{Zr}_y\text{O}_2$. The electron diffraction pattern analysis of a selected area of this sample (Figure S6-C) concludes the crystallographic analysis of the specimen, revealing reflections corresponding to the crystal planes of the oxides. This underscores a coexistence of all investigated species within the nanoparticle aggregates as suggested from the TPR-TGA analysis (Fig. 3).

As concluded from the of N_2 -physisorption isotherm analysis

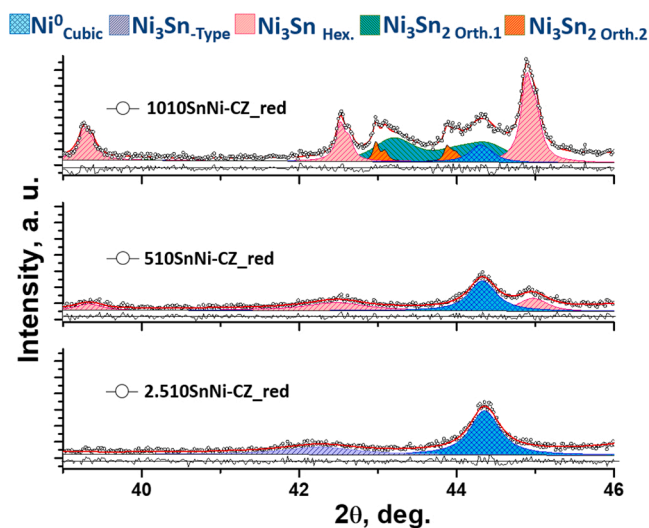


Fig. 2. : Magnification of the 2θ region between 39° and 46° showing the different crystal structures of the metallic and intermetallic $\text{Ni}^0/\text{Ni}_x\text{Sn}_y$ species of the reduced bimetallic catalysts. The different colored areas show the contributions to the overall Rietveld refinement (red line).

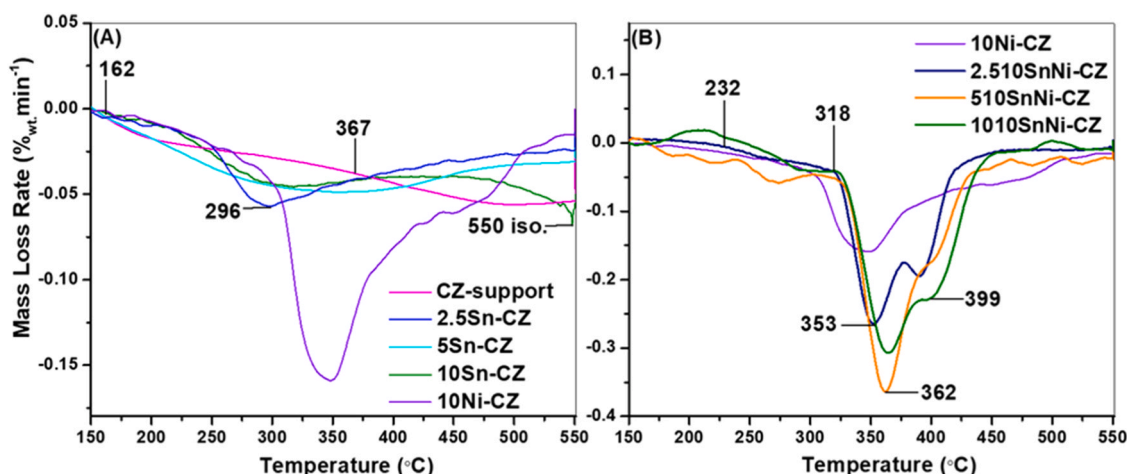


Fig. 3. : Differential thermogravimetric curves (DTG), describing the mass loss rate as a function of temperature, for the monometallic oxidized catalysts (A) and a relative comparison between oxidized bimetallic and the nickel monometallic catalyst (B).

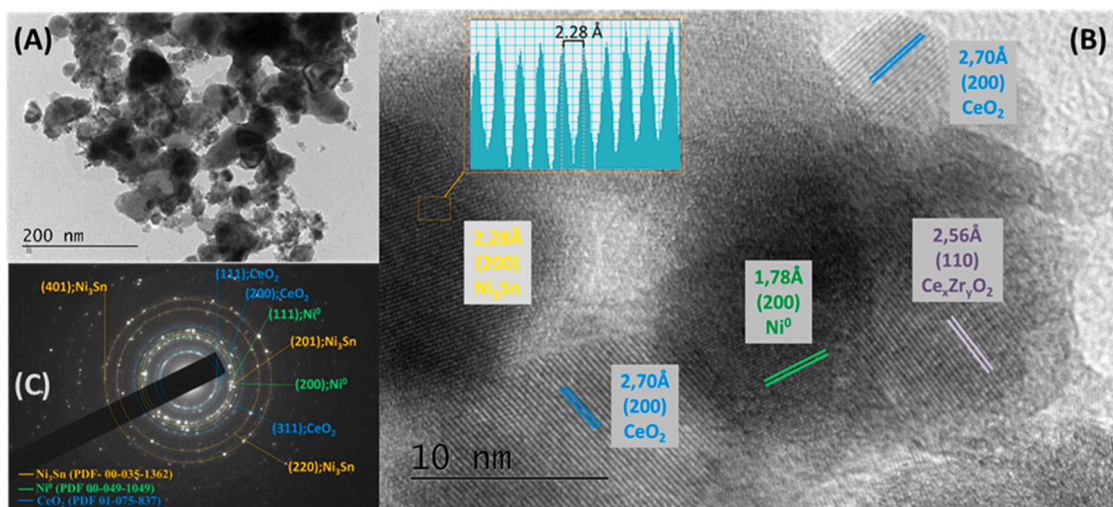


Fig. 4. : TEM images of the sample 510SnNi-CZ_red. (A) 40k magnification. (B) 600k magnification. (C) SAED pattern.

(Figure S1), reduction induces textural changes in the materials, and the relative increase in crystallite size is associated with particle agglomeration (XRD, Table S2). This is confirmed by the low-magnification TEM image in Fig. 4-A, which shows the presence of a cluster of particles with variable sizes and with an increased presence of particles between 20 and 45 nm in size compared to the catalyst in the oxidized state, and even a relatively high number of particles having sizes above 50 nm (Figure S-H). The particles no longer appear quasi-spherical and well defined as in Figure S6-A, but instead take on jagged and less defined contours and higher electron contrast. This textural change is consistent with the reduced desorption of nitrogen at $p/p_0 > 0.95$, indicating a decrease in intra-particle macroporosity associated with particle coalescence. Within this broad distribution, the selected HR-TEM image (Fig. 4-B), reveals the vicinal coexistence of particles of CeO₂, Ce_xZr_yO₂, Ni⁰ and Ni₃Sn IMC, characterized by their crystallographic planes (200), (110), (200) and (200) respectively. The selected area electron diffraction (SAED; Fig. 4-C) pattern corroborates the analysis of the 510SnNi-CZ_red sample. The reflection pattern, generated by the polycrystalline assemblage, demonstrates the vicinal coexistence of well-crystalline Ni⁰ and Ni₃Sn particles, consistent with XRD analysis.

A similar morphological explanation applies to the 2.510SnNi-CZ_red catalyst, as shown in Figure S7. In the low-magnification

image of a sample region (Figure S7-A), there are noticeable assemblies of particles with diverse sizes. The electron diffraction pattern from the same region (Figure S7-C) confirms the presence of CeO₂, Ni⁰, and Ni₃Sn, consistent with the observations in the 510SnNi-CZ_red sample. Furthermore, the high-resolution Figure S7-B reveals an area with the coexistence of crystallographic planes associated with Ni⁰, hexagonal Ni₃Sn, cubic Ni₃Sn (nisnite, PDF-96-901-4007), and a portion of a particle exhibiting crystallites of cassiterite. This highlights the distorted and non-uniform structure of Ni₃Sn in this sample, as indicated by XRD analysis. It also suggests an incomplete reduction of the stannic phase or its passivation, particularly in the vicinity of the metallic and intermetallic phases of the sample. The 1010SnNi-CZ_red sample shown in Fig. 5-A and B, appears as an aggregate of sparse particles with sizes ranging between 50 and 155 nm, adorned with clusters of particles ranging in size from 5 to 25 nm (Figure S-H). The visible disproportion in particle size is indeed consistent with the average crystallite size found by XRD for this sample, particularly concerning the Ni₃Sn₂ IMC crystallites with sizes of 42.4 and 107 nm (Table S2). The Fast Fourier Transform (FFT) shown in the inset of Fig. 5-C recognizes the region of interest within one of the larger particles as being composed of the orthorhombic Ni₃Sn₂ phase. The electron transparency of the borders of this particle allows us to observe a layer of approximately 2 nm thickness of amorphous phase, decorated with small particles of CeO₂

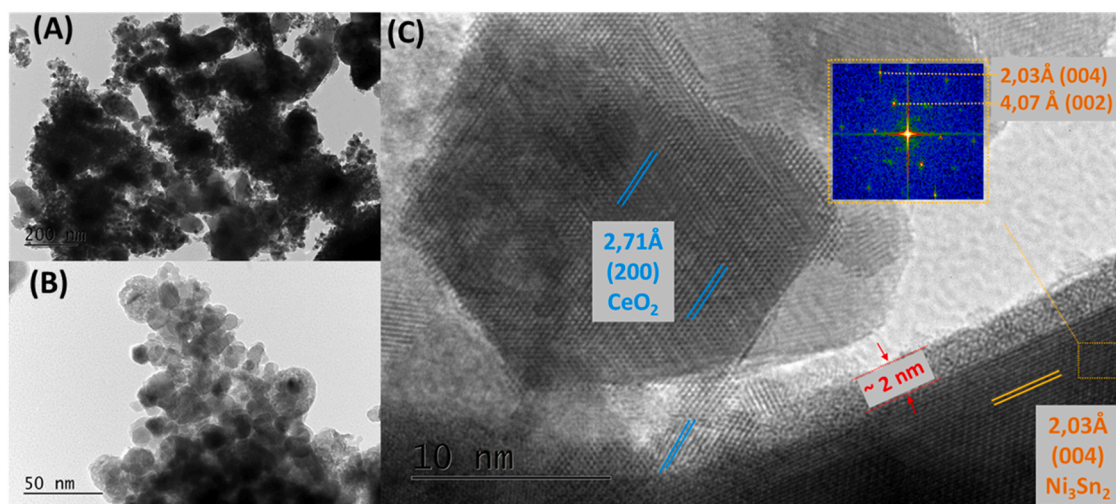


Fig. 5. : TEM images of the sample 1010SnNi-CZ_red. (A) 40k magnification. (B) 100k magnification. (C) 600k magnification.

adhering to the surface.

3.2. ^{119}Sn - Mößbauer, X-ray absorption and X-ray photoelectron spectroscopies

^{119}Sn -Mößbauer spectroscopy was used to analyze in detail the local environments of the Sn nuclei contained in the samples and to thus obtain precise information on the tin phases. In Fig. 6, the Moessbauer spectra are shown and the parameters of the samples under study, i.e.: isomer shift (IS), quadrupole splitting (QS), full width at half-maxima (Γ) and the relative area fraction of each component obtained from the least squares fitting, are summarized in Table 2. All bimetallic catalysts in their oxidized state (Fig. 6-A) exhibit a single component with

isomer shift IS close to 0 mm/s associated with $^{119}\text{Sn}^{4+}$. This IS value and the quadrupole splitting of about 0.6 mm/s can be attributed to SnO_2 particles [28]. In Fig. 6-B, the spectra associated with samples 2.510SnNi-CZ_red and 510SnNi-CZ_red, both show a reduced area fraction of this Sn^{4+} with relative amounts of 28.1% and 10.6%, respectively, with IS at about 0 mm/s that may be associated with unreduced Sn (IV) due either to strong interaction with the catalytic support lattice or to passivation processes. The second contribution present in both mentioned samples concern a singlet at IS of about 1.53 (2) mm/s with relative amount equal to 71.9% for the lowest tin content sample and 89.4% for the highest tin content sample (Table 2). This singlet can be clearly assigned to the presence of the Ni_3Sn IMC [29]. According to the study conducted by Leidheiser et al. [30], the values of

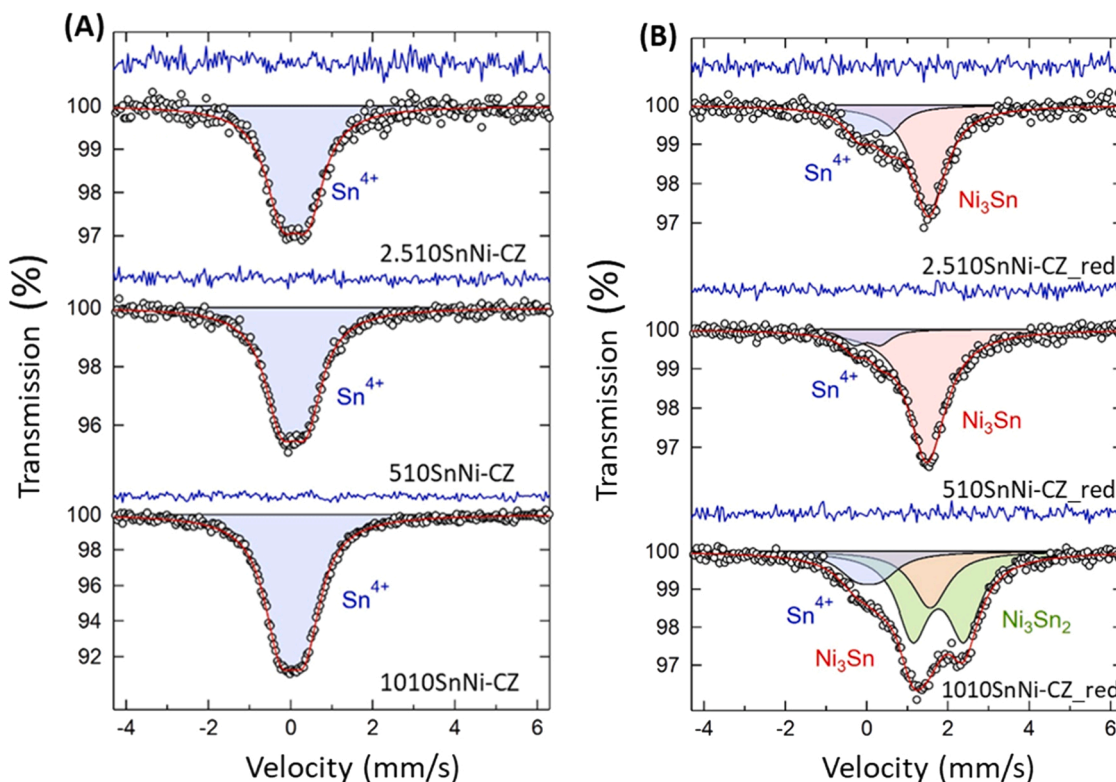


Fig. 6. ^{119}Sn -Mößbauer spectra of the oxidized (A) and reduced (B) bimetallic catalysts. Experimental data points are shown as white spheres, the overall fit as red line, the difference as blue line, and the sub-spectra are shown as red/blue/green singlets/doublets.

Table 2Parameters used to fit the ^{119}Sn Mößbauer spectra: isomer shift IS, quadrupole splitting QS, and line width Γ are given in mm/s.

Sample		IS	QS	Γ	area fraction
2.510SnNi-CZ	$\text{Sn}^{4+}(\text{SnO}_2)$	0.12 ± 0.01	0.63 ± 0.02	0.96 ± 0.02	100.0%
510SnNi-CZ	$\text{Sn}^{4+}(\text{SnO}_2)$	0.09 ± 0.01	0.62 ± 0.01	0.95 ± 0.02	100.0%
1010SnNi-CZ	$\text{Sn}^{4+}(\text{SnO}_2)$	0.06 ± 0.01	0.60 ± 0.01	0.94 ± 0.01	100.0%
2.510SnNi-CZ_red	Ni_3Sn	1.55 ± 0.01	-	0.98 ± 0.04	71.9%
	$\text{Sn}^{4+}(\text{SnO}_2)$	0.18 ± 0.04	0.70 ± 0.06	0.85 ± 0.11	28.1%
510SnNi-CZ_red	Ni_3Sn	1.50 ± 0.01	-	1.11 ± 0.02	89.4%
	$\text{Sn}^{4+}(\text{SnO}_2)$	0.03 ± 0.04	0.63 ± 0.05	0.63 ± 0.11	10.6%
1010SnNi-CZ_red	Ni_3Sn_2	1.78 ± 0.02	1.26 ± 0.03	0.93 ± 0.05	58.6%
	Ni_3Sn	1.58 ± 0.03	-	1.06 ± 0.18	23.2%
	$\text{Sn}^{4+}(\text{SnO}_2)$	0.06 ± 0.05	0.59 ± 0.09	1.11 ± 0.15	18.2%

isomer shift in the Sn-Ni compounds, undergo a linear decrease, compared to that of the β -Sn phase ($\text{IS} = 2.5 \pm 0.06$ mm/s), as the nickel concentration increases. This phenomenon is due to a delocalization of the s-electron density of the tin nucleus within the conduction d-band of the intermetallic compound with consequent depopulation of the 5 s orbitals of tin as the average number of neighboring nickel atoms increases.

Also in the same figure, the results of sample 1010SnNi-CZ_red can be rationalized by deconvoluting the experimental data into three main contributions. The first contribution at $\text{IS} = 0$ mm/s and $\text{QS} = 0.59$ mm/s again comes from Sn^{4+} ascribable to a relative amount of 18.2% of the signal. The second contribution is represented by a singlet at $\text{IS} = 1.58 \pm 0.03$ mm/s with relative quantity equal to 23.2%, which, as already described, can be associated with the hexagonal Ni_3Sn . The third and most dominant contribution in this sample, is described by the doublet at $\text{IS} = 1.78 \pm 0.02$ mm/s with $\text{QS} = 1.26 \pm 0.03$ mm/s, with area fraction of 55% and attributed to Ni_3Sn_2 [31].

Beyond supporting the XRD (Fig. 2) and TEM (Figs. 4, S7 and 5) results, ^{119}Sn - Mößbauer spectroscopy, which makes use of transitions from excited nuclei with $I = 3/2$ to the ground state ($I = 1/2$), is particularly sensitive to electric field gradients at the sites of the Sn nuclei. The presence or absence of quadrupolar splitting of the Mößbauer lines indicates the nature of the electronic environment, which can be related to the symmetry of the crystalline environment of the tin nuclei. According to Silver et al. [32] the presence of a singlet in the Ni_3Sn IMC can be explained by the fact that in this intermetallic compound, the tin atom occupies a trigonal bipyramidal site between two planar rings of three equally spaced nickel atoms [32], which gives the Sn sites in this structure a high crystallographic and electronic symmetry. In contrast, in the Ni_3Sn_2 IMC, the tin is occupying a bipyramidal site with high crystallographic symmetry, but possesses a stoichiometrically high tin deficiency composition, where each tin atom is surrounded by six nearest nickel atoms, but each nickel atom is surrounded by four tin atoms. This asymmetric distribution of atoms in the crystalline lattice generates an unsymmetrical electronic distribution that is reflected by a quadrupolar splitting and thus a doublet in the Mößbauer spectrum [32]. The combination of information derived from the isomer shift and the magnitude of the quadrupolar splitting provides insight into the degree of charge transfer $\text{Sn} \rightarrow \text{Ni}$ in the intermetallic compounds. This interaction is particularly predominant in the Ni_3Sn_2 IMC of the 1010SnNi-CZ_red sample.

Further evidence of these charge transfers can be observed by superimposing the normalized X-ray absorption spectra at the Ni K-edge of selected samples in their reduced and post-passivated state, in comparison with references of known composition, as shown in Fig. 7.

The near edge region of XAS spectra, referred to as XANES (X-ray absorption near edge spectroscopy), elucidates the local electronic environment of absorbing nickel atoms (Fig. 7-A). A gradual decrease in the intensity of the Ni^0 absorption edge at 8333 eV is observed, accompanied by an increase in the energy of the absorption onset, which in the sample with the highest tin content (and highest presence of Ni_3Sn and Ni_3Sn_2) is located at 8340 eV (pre-edge inset Fig. 7-A). Similar

values and shapes of the XANES region of these materials have been reported by Onda et al. [27], specifically of the adsorption edge at 8340 eV. Its intensity has been shown to be dependent on the tin content in the IMCs, but also could be attributable to particle size or support effects [33,34].

From the Fourier transform of the real space (R) of the EXAFS spectra (Fig. 7-B), it is evident a clear difference in the bonding distances between the reduced catalysts and the NiO reference, emphasizing that the reduced catalysts display a significant contribution at the coordination shell corresponding to Ni-M scattering ($M = \text{Ni}$ or Sn). Both 10Ni-CZ_red and the reduced bimetallic catalysts also exhibit a small contribution at $R \approx 1.5$ Å (not phase corrected and ≈ 2 Å phase corrected), which can be associated with the Ni-O scattering path (Figure S8-A, Table S3). Noteworthy is the observed variation in $\chi(k)$ peak intensities across the samples in the reciprocal k-space shown in Figure S8-B. This variation shows a decreasing trend with increasing tin content, reaching minimum intensity values in 1010SnNi-CZ_red. The sample with the highest tin concentration, being the only one to have also large aggregates of Ni_3Sn_2 in respect to the other samples, exhibits a particularly unique structure in the k-space spectra. This fact, suggests a different atomic arrangement of nickel atoms in the sample, potentially implying a speculative but complementary connection to what was mentioned in the analysis of isomer shifts via ^{119}Sn -Mößbauer spectroscopy on tin nuclei in the Ni_3Sn and Ni_3Sn_2 IMCs (Fig. 6). Assuming, therefore, an electron transfers from Sn to Ni, it is plausible that the density of the occupied states near the nickel K-edge increases, leading to a decreasing in X-ray absorption due to an increase of the absorption edge energy and to a lower probability of electronic transition between occupied and unoccupied states. It is also necessary to consider that such variations in the EXAFS oscillations, can be influenced by passivation layers on the particles, which on the other hand, are present in all the catalysts under study so that the additive possibility of the two effects cannot be excluded.

In relation to the oxidized component on the surface of the Ni_xSn_y particles, Fig. 8 displays the spectra obtained from the investigation of Ni 2p_{3/2} and Sn 3d core levels using X-ray photoelectron spectroscopy of the surface of the reduced bimetallic catalysts. The Ni2p_{3/2} core level region (Fig. 8-A), shows in all samples the peak at BE at 855.8 eV with an associated shake-up peak belonging to Ni^{2+} and with BE 852.8 eV the contribution of Ni^0 with a decreasing area depending on the tin content in the samples [35]. The Sn3d core level region also shows an oxidized portion located at BE 486.6 eV belonging to Sn^{4+} and a contribution from Sn^0 located at BE 485.0 eV [36]. Table S4 shows the concentrations of all the atomic species present in the specimens. Sample 1010SnNi-CZ_red compared to the other samples, while having the same Ce/Zr molar ratios, has a higher surface concentration of cerium and zirconium but not a proportionally high amount of tin and nickel. This fact could be explained by the evidence gathered via TEM and XRD about the disproportionate difference in size of the particles and crystallites constituting this sample (Fig. 5 and Table S2). Some interesting observations stem from the data shown in Table 3, concerning the normalized percentage ratios of Ni, Ni^0 and Sn^0 species on the surface of

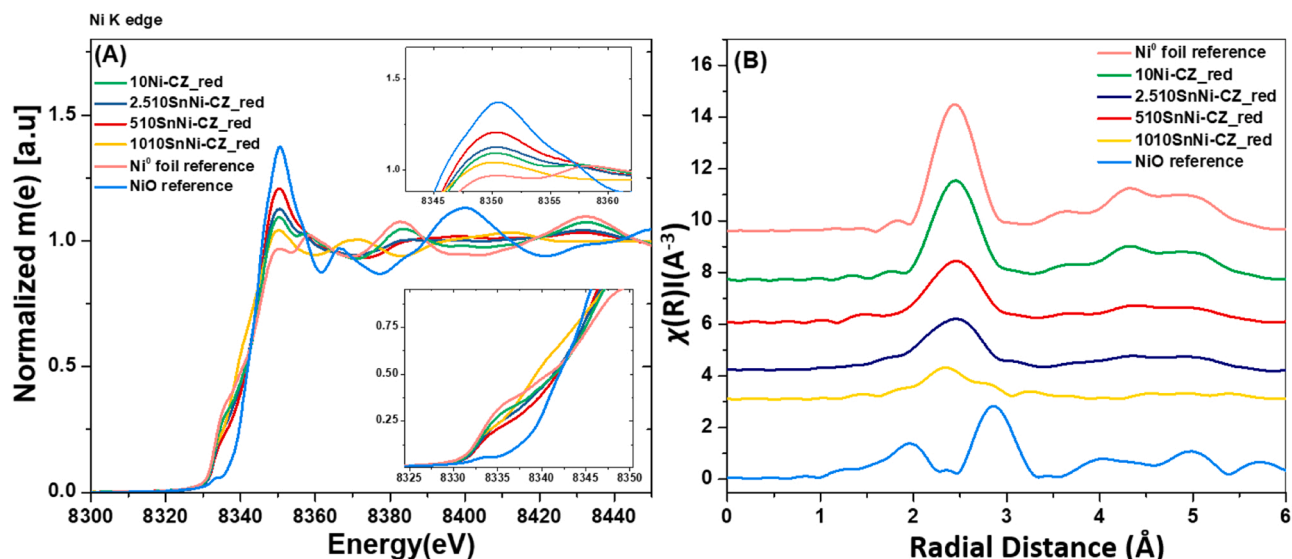


Fig. 7. : Normalized Ni K-edge XANES spectra (A) of reduced and afterwards passivated Ni-containing samples in comparison with Ni foil, NiO and k^3 -weighted Fourier Transforms of EXAFS spectra (B).

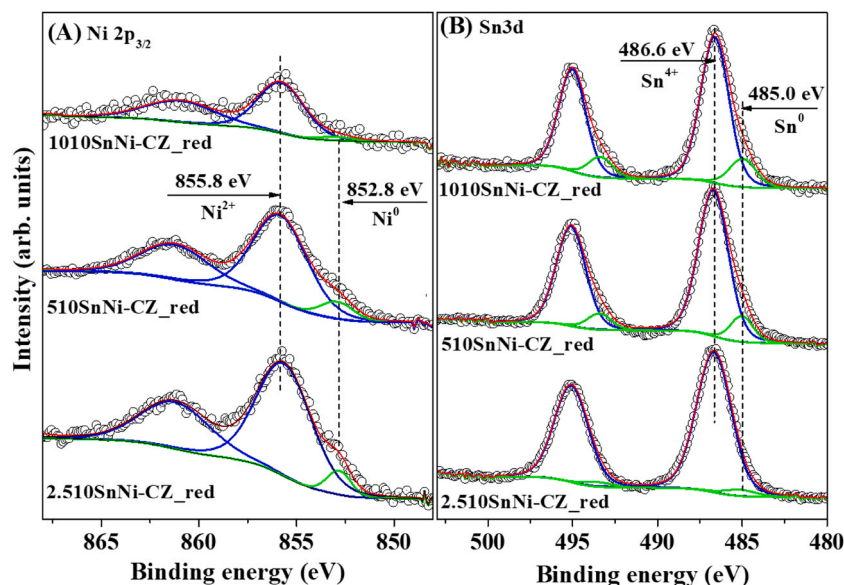


Fig. 8. : XPS spectra of the Ni 2p_{3/2} core level (A) and Sn 3d core level (B) for the reduced bimetallic samples.

Table 3

Surface concentrations of Ni, Ni⁰ and Sn⁰ in normalized atomic percentages obtained via XPS.

Sample	Ni/(Ni+Sn) x 100	Ni⁰/(Ni⁰+Ni²⁺) x 100	Sn⁰/(Sn⁰+Sn⁴⁺) x 100
2.510SnNi-CZ_red	76.4	5.8	10
510SnNi-CZ_red	67.8	7.4	11.8
1010SnNi-CZ_red	50.5	3.4	15.5

the catalysts. In fact, as already predicted from the deconvolution of the spectra in the 2p_{3/2} core level region, the surface of the samples seems to become depleted of nickel as the tin content in the samples increases. Furthermore, it is possible to note that even though a considerable oxidized component is present in all the samples for both Sn and Ni, the Sn⁰ component maintains an almost linear distribution on the catalyst surfaces, compared to that of Ni⁰. The latter in the 510SnNi-CZ_red

sample would appear to exhibit a concentration of the metallic portion slightly higher even than the one found for the catalyst with the lowest tin content. The presence of a passivation layer or/and even a surface metal interface enriched with tin atoms in the Ni_xSn_y IMCs is not an entirely new behavior of these compounds.

In fact, recently a study of these interfaces under controlled conditions conducted by Mauri et al. [36] reported that in oxygen-rich environments (including air), these surfaces are prone to oxidation with enthalpies below -280 kJ/mol and that furthermore on these bimetallic surfaces, a selective oxidation of nickel often occurs with migration of NiO towards the surface, leading to a stratification of the exposed atomic species on the surface of the different IMCs. This mechanism of migration and selective oxidation of surface atoms would be consistent with what was observed from the XPS data of the present work and contextually supported by the experimental evidence described so far.

Table 4

Ni and Sn loadings, hydrogen uptake and exposed surface area of the nickel active sites*.

Sample	Ni (wt%)*	Sn (wt%)*	H ₂ uptake (μmol/g)	Exposed active metal surface area (m ² /g _{cat})	Exposed active metal surface area (m ² /g _{Ni})
10Ni-CZ	10.2	-	37.3	2.91	33.90
2.510SnNi-CZ	10.3	2.6	11.1	0.87	10.09
510SnNi-CZ	10.1	5.3	12.3	0.96	11.18
1010SnNi-CZ	10.0	9.6	5.5	0.43	5.05
CZ-support	-	-	-	-	-

* H/Ni adsorption stoichiometric factor of 1 was used.

** Determined by LA-ICP-MS

3.3. H₂ chemisorption analysis

Taking into account what was introduced in the "preamble to the H₂ chemisorption analysis" (section 8 of the SI) and the studies by Knozinger et al. [37] and Hammer et al. [38], in Figure S9, hydrogen chemisorption isotherms obtained from similar quantities of the pre-reduced nickel-containing catalysts are shown. The catalyst containing only supported Ni nanoparticles (10 wt%) exhibits the highest H₂ uptake with a dispersion calculated to be 5% and an exposed active metal surface of approximately 33.9 m²/g_{Ni} (Table 4). The formation of intermetallic compounds with tin, however, drastically decreases the quantity of H₂ uptake with a trend, though not perfectly linear, dependent on the increase of tin in the samples. Similar behavior with a mitigation of the chemisorption properties has also been found in a wide range of Sn-containing IMCs (examples are Ni_xSn_y [27], Pt_xSn_y [39] and Pd_xSn_y [40]). Like copper and gold, tin also has fully occupied d orbitals (Sn = [Kr] 4d¹⁰ 5s² 5p²) and has no activity for hydrogen chemisorption. In addition to the intrinsic inertness of tin for the reaction under examination, it should be remembered that the ¹¹⁹Sn-Möbbauser analysis revealed the electron donation of the 5s orbitals of the tin nuclei, in favor of the d-band of the nickel. As previously noted, the electronic effects of the interaction of the adsorbate (H₂ in this case) with the electron density of the d-band determine the positioning and occupation of the antibonding state with respect to the Fermi level, energetically favoring or disfavoring H₂ chemisorption. Although simplistic, it is logical to assume that in a sample like 1010SnNi-CZ_{red}, where two IMCs are more abundant, the limitation of nickel's chemisorption properties is highest due to extended electron donation from Sn→Ni to a wider distribution of nickel atoms.

Similar to the 1010SnNi-CZ_{red} sample, the bimetallic catalysts with lower tin loading show intermediate H₂ uptake values (11.0 and 12.2 μmol/g), with active exposed nickel areas equal to almost one third of the monometallic nickel catalyst (Table 4). While admitting that an intermetallic compound such as Ni₃Sn has limited chemisorption properties, the experimental values obtained from the analysis reflect a considerable decrease in the exposed active metallic nickel. The chemisorption properties of hydrogen in the 2.510SnNi-CZ_{red} sample, were also unexpectedly found to be slightly lower than those for the 510SnNi-CZ_{red} one, despite having a lower relative amount of Ni₃Sn due to the lower loading of tin in the sample. Besides, the measurement of the average size of the crystallites calculated by XRD for Ni⁰ clearly shows twice the Ni crystallite size for the 510SnNi-CZ_{red} sample compared to the 2.510SnNi-CZ_{red} (21 nm and 42.6 nm, respectively; Table S2). Therefore, the former sample should be the less active of the two considered above, because of both its higher relative concentration of hexagonal Ni₃Sn, and of the larger crystallite size and hence smaller exposed surface area of the Ni⁰ particles available for chemisorption. However, in agreement with what is shown and described by other characterization techniques such as XRD (Fig. 2), HR-TEM (Figure S7), XPS (Fig. 8), a possible explanation for the reduced H₂ chemisorption capacity for the 2.510SnNi-CZ_{red} catalyst, could lie in the fine dispersion of the nixtite Ni₃Sn in the 2.510SnNi-CZ_{red} sample, compared to the more crystalline hexagonal Ni₃Sn for the 510SnNi-CZ_{red} sample, that could form an higher coverage of the smallest metallic nickel

crystallites, and thus lowering their reactivity.

3.4. Catalytic results of the ethylene glycol (EG) 6%_{wt}. aqueous phase reforming

The catalytic tests were conducted in a batch reactor after reduction and passivation for all mono- and bimetallic catalysts, following the parameters described in Section 2.3. Note, that the catalytic tests reported in this study were carried out inside the closed volume of an autoclave, which lead to the accumulation of a liquid phase mostly composed of protic molecules. With reference to the initial conditions will be named, neutral conditions the experiments starting with an initial pH_i = 7, and alkaline conditions the ones starting with an initial pH_i = 14. The pH values, in both cases were found to be drastically lowered at the end of the reactions. Specifically, the final pH values found after the tests carried out in neutral initial conditions resulted to be between 4 and 3, while for the tests conducted in alkaline initial conditions a final pH of 8 was recorded for the samples with the lowest feed conversion and 7 for those with the highest activity.

3.4.1. Catalytic behavior of monometallic Sn-containing catalysts under neutral and alkaline conditions

Fig. 9 summarizes the conversion levels of ethylene glycol, selectivity to H₂ and CH₄, and conversion to gas-phase products of the reduced monometallic tin catalysts under neutral and alkaline reaction conditions.

The APR reaction of 6 wt% EG on the surface of monometallic tin catalysts dispersed on ceria-zirconia, although exhibiting low conversion values (maximum approx. 12% for the 5Sn-CZ_{red} sample) at neutral conditions, allow attention to be focused on several peculiarities of the reaction mechanism. The EG conversion depends strongly on the initial pH of the reaction. The samples tested in alkaline conditions show a doubling in feed conversion and H₂ yield compared to those processed under initial neutral conditions. Another interesting data that could be extrapolated from the analysis of the gaseous phase Figure S10, is the lowering of the yield of carbonaceous products in the gaseous phase and the complete absence of CO₂ and CO for the samples tested in an alkaline environment (Figure S10-B) compared to the large portion that the same gases represent in the gaseous component produced by the catalysts in an initial neutral environment (Figure S10-A). Again, in Figure S10, it is possible to see how in both process conditions, the gaseous phases produced also contain CH₄, C₂H₆ and C₃₋₄₊. The latter appear to be the main components of the carbonaceous gas phase of the alkaline process. Based on literature, to be able to form the registered gaseous phase composition, the reaction pathways could preferentially pass through the formation of acetaldehyde, which being particularly reactive can lead to: 1) Oxidation with formation of acetic acid. 2) Hydrogenation of acetaldehyde with the formation of ethanol or ethane. 3) Self-condensation with formation of C_{2+x}-OH and their subsequent reforming into C₄ and C₃ alkanes and alcohols [41]. This combination of processes, later shown in Scheme 1, can also contribute to methane production.

Each of these three hypotheses, albeit simplistic, is selectively well represented by the histograms in Figure S10. While it was possible to

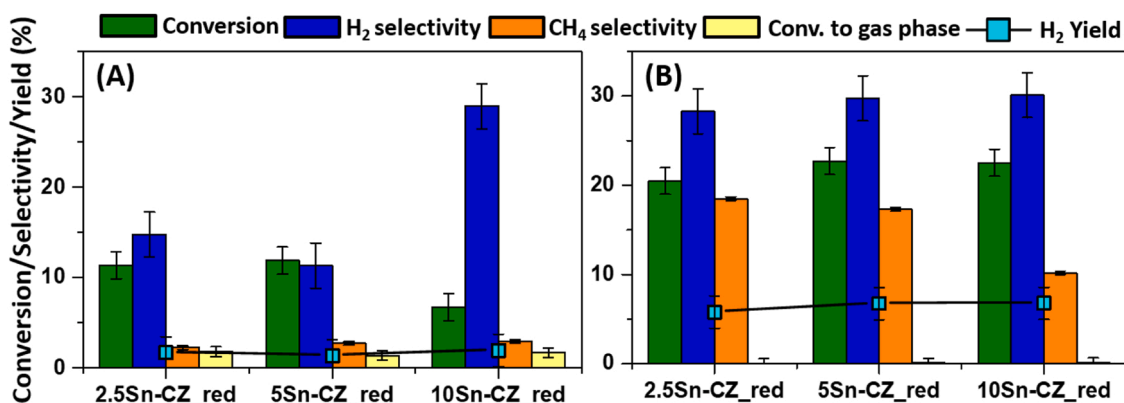


Fig. 9. : Histograms summarizing the conversion of EG, the conversion of EG into gas phase, the yield of H₂ obtained and the selectivity to H₂ and CH₄; for reactions carried out under neutral (A) and alkaline (B) conditions. The error bars represent the standard deviation of the experiments.

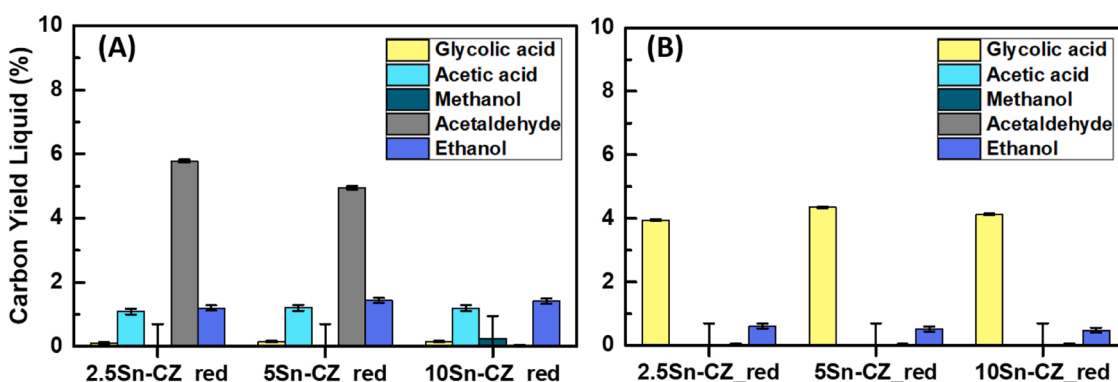


Fig. 10. : Carbon yield to main liquid products obtained from the monometallic reduced tin catalysts at neutral (A) and alkaline conditions (B). The error bars represent the standard deviation of the experiments.

find traces of these three pathways for the 2.5-/5Sn-CZ_{red} catalysts at neutral conditions (Fig. 10-A), with the presence of small quantities of acetaldehyde, acetic acid and ethanol in the liquid phase, partially justifying the C₃₋₄ alkanes in the gas phase, the liquid phase of the tin-based catalysts tested in alkaline environment show mainly the formation of glycolic acid, combined with a wide distribution in traces of alcohols and polyols such as: 1-propanol, 1,2-propanediol, 2,3-butanediol, 1,2-butanediol (not shown in the histograms). The preponderant presence of glycolic acid together with an increase in feed conversion, a higher selectivity to hydrogen and absence of CO₂, highlights the presence of a reaction mechanism of ethylene glycol under initial alkaline

conditions, different from the one established in literature [6,29], but capable (at least for a tin-only active phase) of increasing EG conversion and hydrogen yield by bypassing the WGS reaction and the direct cleavage of the feed. The homogeneous nature of this reaction is evident from the gas phase product distribution obtained from the blank test in alkaline environment, the results of which are shown in Table S5. This alkali-induced homogeneous process, elucidated later in this study as a disproportionation of the EG, is significantly enhanced and related to the precursory EG oxidation, heterogeneously mediated by a catalyst.

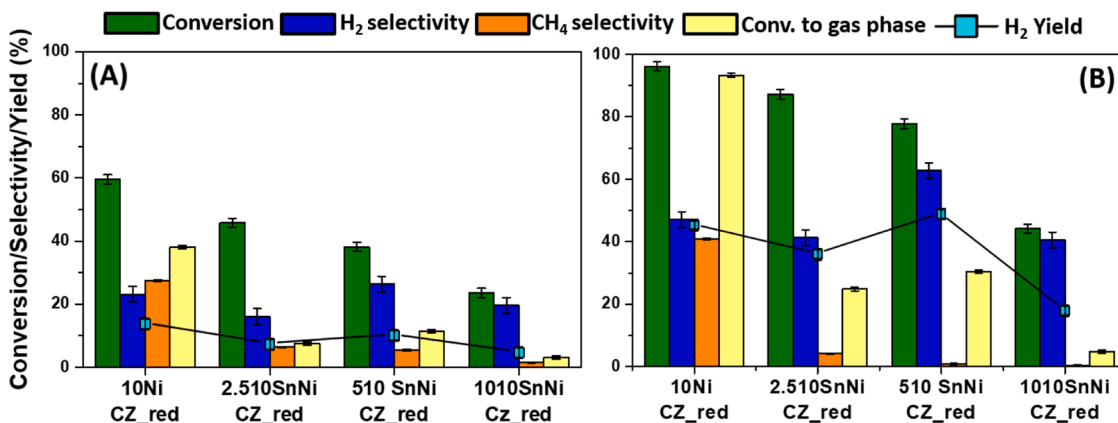


Fig. 11. : Histograms summarizing the conversion of EG, the conversion of EG into gas phase, the yield of H₂ obtained and the selectivity to H₂ and CH₄ for the bimetallic catalysts for reactions carried out under neutral (A) and alkaline (B) conditions.

3.4.2. Catalytic behavior of Ni and Ni_xSn_y catalysts in APR of ethylene glycol at neutral and alkaline conditions

The catalytic performance of the monometallic catalyst 10Ni-CZ_red will be discussed together with the bimetallic catalysts for better visibility and comparison of the obtained results. In Fig. 11, EG conversion, H₂ and CH₄ selectivity, H₂ yield and EG conversion to gas phase, under initial neutral and alkaline conditions are summarized. At neutral conditions, the monometallic nickel catalyst shows highest EG conversion level, while for bimetallic catalysts the conversion levels decrease with increasing tin content. At the same time, the high methane selectivity observed for the 10Ni-CZ_red catalyst at neutral conditions has a gradually decreasing trend with increasing tin loading (Fig. 11-A).

As in the case of monometallic tin catalysts, the reaction carried out under alkaline conditions (initial pH 14) led to a considerable increase in the conversion of ethylene glycol for all the catalysts (Fig. 11-B). For the catalyst containing only nickel, the increase in conversion was about 36% (about 96% of the converted feed) of which almost 93% of the products in gas phase. The conversion trend of the bimetallic catalysts has a distribution dependent on the tin content similar to the reactions under neutral conditions, but with an increase in EG conversion of approximately 50% for all catalysts, with a maximum value of about 83% of EG converted achieved by the catalyst with the lowest tin content (2.510SnNi-CZ_red). The methane and H₂ selectivities for the 10Ni-CZ_red sample under alkaline conditions was 20% higher than at neutral conditions because of the higher EG conversion. Furthermore, the higher conversion for the bimetallic catalysts seems not to significantly influence the selectivity to the methanation reaction. For these samples, the cleavage mechanisms (at least in gas phase, Fig. 11-B) appear to be relatively hydrogen-productive, culminating with an H₂ yield of about 50% for the 510SnNi-CZ_red sample under these conditions. The latter assertion can be confirmed by the distribution of the carbonaceous products in the gas phase (Figure S11-B), where a selectivity of the bimetallic catalysts to CO₂ higher than 90% is observed, derived from the water-gas shift reaction (WGS, Eq. 2), in contrast to what was observed for the monometallic tin samples.

As for the monometallic tin catalysts, the bimetallic catalysts show lower gas phase selectivities and yield of carbon to gas than for the 10Ni-CZ_red sample (Figure S11A-B). At neutral conditions, the presence of gaseous products with more than two carbon atoms (C₃₋₄₊), with increasing selectivity as a function of the amount of tin in the samples, suggests aldol condensation reactions with the formation of products with a longer carbon chain than the feed. A substantial difference found in the liquid product distribution (Fig. 12-A) is the absence of acetaldehyde for the Ni-Sn combinations (as for the Sn monometallic at neutral conditions, Fig. 10-A), but instead ethanol derived from direct hydrogenation and acetic acid derived from oxidation are produced.

The composition of the liquid phase of the products from the reactions under alkaline conditions is presented in Fig. 12-B. Although the reduced gaseous carbon yield led to a broad range of trace condensation products, the major constituents of the liquid phase are represented by glycolic acid and methanol. While no glycolic acid was found for the 10Ni-CZ_red catalyst, the liquid carbon yield of the alpha-hydroxy acid selectively reaches 25% for the catalyst with the highest tin content.

3.5. Rationalization of the EG cleavage pathways under the different studied conditions

For a clearer understanding of how the selection of active metallic and intermetallic phases impacts the cleavage pathways of ethylene glycol under neutral and alkaline initial pH conditions, we propose the mechanism outlined in Scheme 1.

The catalytic data shown in the previous section are the results of a complex combination of factors that must be taken into consideration to understand what happens on the surface of the catalytic system in the APR reaction in batch conditions. It is evident how the presence of tin and nickel in the samples combines the intrinsic catalytic qualities of the two metals, depending on the distribution of the metallic and intermetallic species in the catalysts. Although the bimetallic reduced catalysts present similar exposed surface areas in the range $51 < \text{BET} < 57.5 \text{ m}^2/\text{g}$; Table 1, their catalytic behavior under neutral conditions seems linked to the electronic properties of Ni⁰ and of the different combinations of the detected IMCs, Ni₃Sn and Ni₃Sn₂. The initial chemisorption of ethylene glycol on the surface of the metal, takes place with the release of a molecule of H₂ from the feed [29] (path I and II, Scheme 1). The selective formation of one of the two radical adducts of the glycol can be considered the first step which determines the distribution of the products and in part, the yields of the process.

From the analysis of liquid and gaseous phase products at neutral conditions, the 10Ni-CZ_red catalyst favors equally two specific cleavage paths shown in Scheme 1, either path (II) or the combination of paths (I)-(III)-(IV). Path (II) is mostly considered as a hydrogen consuming mechanism leading predominantly to CO₂, CH₄ and ethane production. It is derived from the cleavage of the C-O bond of the EG and the subsequent preferential hydrogenation of the derived tautomer with release of ethanol as the major product in the liquid phase (Fig. 12-A). On the other hand, path (I) is generally considered the hydrogen-productive one. It occurs by breaking the C-C bond of the feed, subsequently what most probably happens is the formation of methoxy groups which can either stabilize in methanol (later found in the liquid phase), or participate in the direct methanation reaction (path IV-a Scheme 1), or undergo first a dehydrogenation, and subsequently an oxidation (WGS, path (III), Scheme 1) with the release of CO₂ and two H₂ molecules in

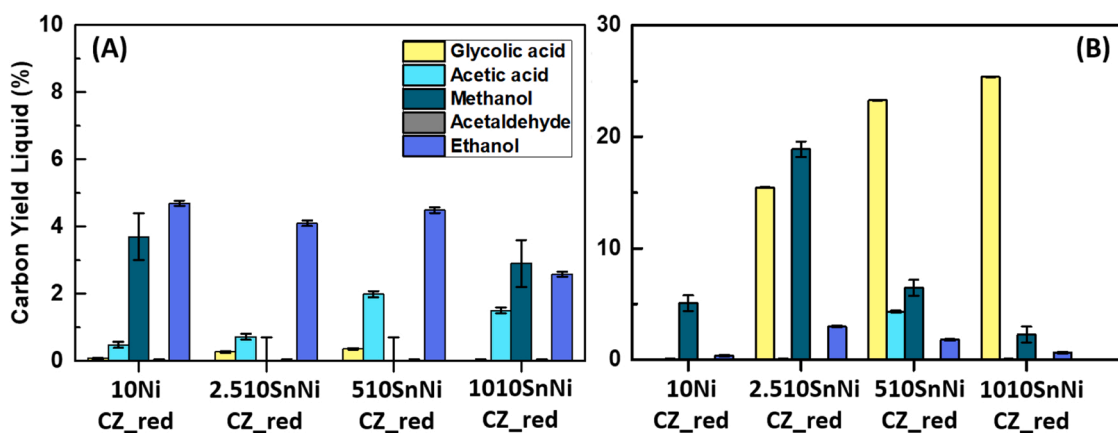
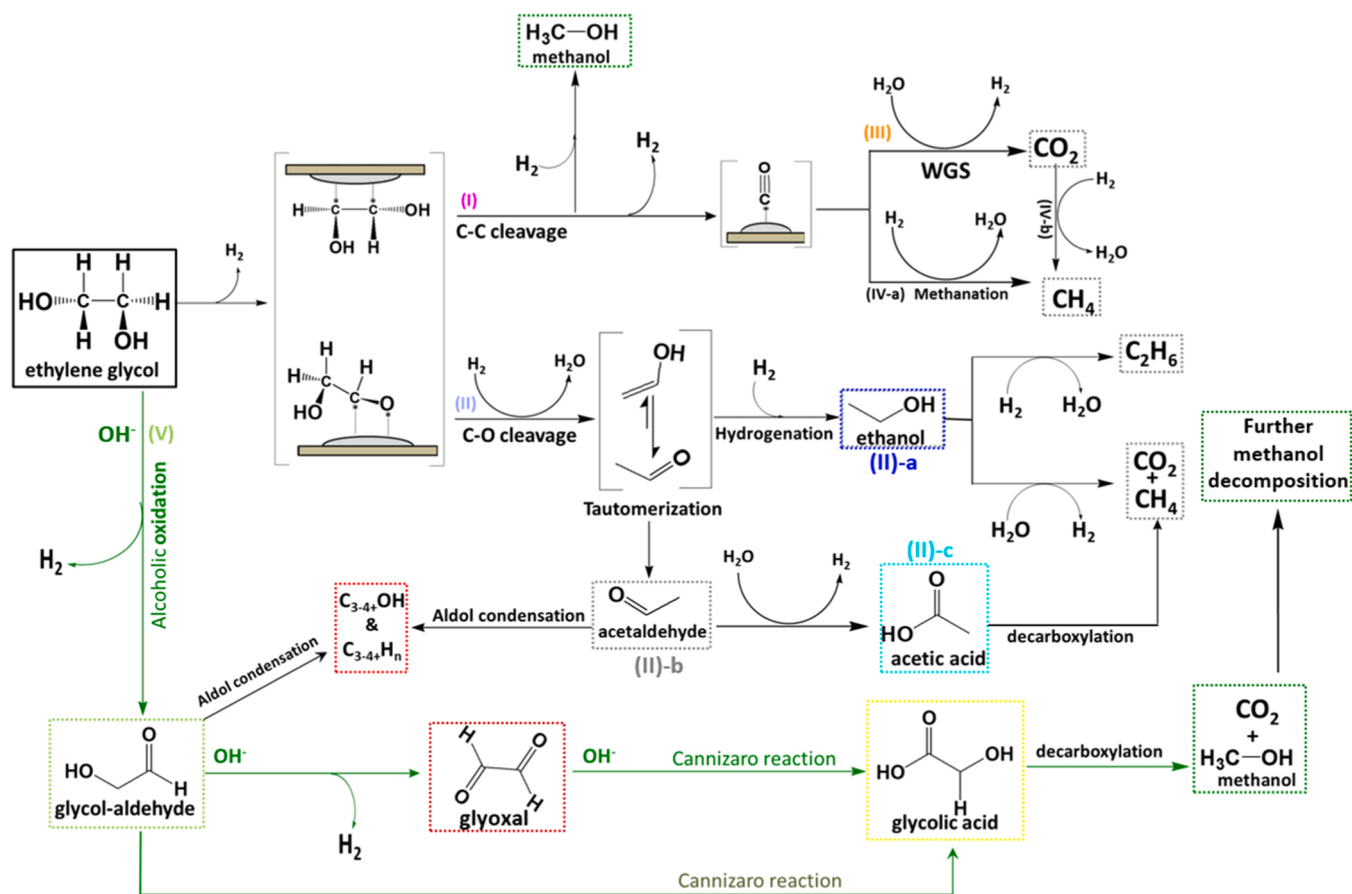


Fig. 12. : Carbon yield to main liquid products obtained from the bimetallic catalysts at neutral (A) and alkaline conditions (B). The error bars represent the standard deviation of the experiments.



Scheme 1. : Proposed mechanism to describe the possible cleavage paths of ethylene glycol during the APR reaction under neutral and alkaline conditions.

total [8,42]. With a particularly high selectivity for nickel, the CO_2 or CO produced by these reactions can further occur in the methanation side reaction (path IV-b Scheme 1), producing a gas-phase mixture with high H_2 , CH_4 and CO_2 contents (Fig. 11 and S11).

While the electronic properties of nickel make its chemisorption and spill-over ability not selective in the studied feed cleavage mechanisms, all monometallic tin catalysts (2.5-, 5- and 10Sn-CZ_red), suffer from the low cleavage rate imposed by the electronic properties of the active metal, itself influenced by the low degree of reduced component of the lowest concentration sample (Fig. 3, DTG) and the large average size of the Sn^0 crystallites found in sample 10Sn-CZ_red (Table S1). In addition to the low feed conversion values obtained at an initial neutral pH (Fig. 9-A), indicative of a low propensity to break the C-H and O-H bond, the distribution of the products in the liquid and gaseous phase suggests that, under these conditions, the monometallic tin catalysts selectively prefer a reactant transformation passing through cleavage of the C-O bond (path II, Scheme 1). For these samples, the radical adducts of the feed preferentially convert to the more stable tautomer, acetaldehyde (Scheme 1, path (II-b)), instead of forming ethanol by hydrogenation. The acetaldehyde product is the main constituent of the liquid phase obtained under neutral conditions from these catalysts (Fig. 10-A), and as it was previously mentioned, it is the precursor of the acetic acid derived from its oxidation and of the long-chain gaseous phase products obtained from aldol condensation (Scheme 1, path (II-c)).

The bimetallic catalysts tested under initial neutral pH, show a catalytic behavior displaying the properties of the two active metals. In this case the nickel seems to act as the first initiator of the reaction, while the tin present in the intermetallic compounds Ni_3Sn and Ni_3Sn_2 and as well in the non-reduced portion (Fig. 6, Figure S5), instead seems to act as a "mitigating agent", gradually reducing the conversion of the feed, as its interaction with nickel increases (Fig. 11-A). The electronic properties of

the metallic and intermetallic phases in the 2.510SnNi-CZ_red and 510SnNi-CZ_red samples, seem to selectively prefer the cleavage path through the breaking of the C-O bond of the feed (path (II) Scheme 1, Fig. 12-A), revealed by the presence of ethanol and acetic acid. Unlike the samples with a lower tin content, the 1010SnNi-CZ_red sample, albeit at low conversion levels, shows a less selective initial cleavage through either the breaking of the C-O bond or the C-C bond of the ethylene glycol which is highlighted by the presence in the liquid phase of both the products of path (I) and those of path (II) (Fig. 12-A and Scheme 1). However, the product distribution from all bimetallic catalysts differs substantially from the behavior of 10Ni-CZ_red, demonstrated by their low selectivity to the methanation reaction. Although all of them are prone to methane-producing pathways, the presence of tin in the samples inhibits the production of methane regardless of the starting reagent to be decomposed (ethanol, acetic acid or methanol). A similar behavior has already been observed by Shabaker et al. [29,43], and it has been attributed, in tin-nickel IMCs, to the suppression of the threefold-hollow sites on Ni (111) which favor the dissociative adsorption of CO , necessary for the methanation reaction. DFT calculation on the activation energy barriers regarding CO dissociation and OH formation in the methanol decomposition reaction developed by Xu et al. [44] defines that tin in the intermetallic Ni_3Sn , possess a higher activation potential barrier for the two reactions than Ni (111). The latter could justify the product distribution in the liquid and gaseous phases of the current study under standard conditions and can be used to correlate the derived results from the H_2 chemisorption analysis with the final hydrogen yields of the reactions as shown in Fig. 11 and Figure S9.

The registered low concentration of glycolic acid produced by the bimetallic catalysts in the APR-EG_{6%} at initial neutral conditions reveal a mechanism which, at neutral pH, is a side reaction of little importance, but in alkaline environment seems to competitively dominate the

cleavage pathway of the ethylene glycol revealed by the dominant presence of glycolic acid (Fig. 12-B).

Glycolic acid (GA) is the simplest of the α -hydroxy carboxylic acids, and currently has a particular use as a raw material in fine chemistry and pharmacy, as well as being the precursor of the poly-glycolic acid (PGA), a polymer with high biodegradability and biocompatibility [45], currently used in the field of surgery and drug-delivery. The formation of this product under the operating conditions of APR in alkaline environment can be explained in relation to what was reported by Zhan et al. [46] in an EG to GA conversion reaction in alkaline environment, catalyzed by iridium or ruthenium complexes (shown in the green path of Scheme 1). The most plausible driving force for this catalytic pathway could be the dehydrogenation of ethylene glycol and subsequent selective oxidation of an alcoholic group to a carbonyl functionalization, then to the production of glycol aldehyde [7] (path (V), Scheme 1).

There are multiple examples of selective oxidation reactions (also called dehydroxylation reactions) of alcohols and diols mediated by heterogeneous catalysts to obtain the related carbonyl compound [47]. An interesting and relevant example is the synergistic effect between silver particles and CeO_2 proposed by Grabchenko et al. [48] in the selective oxidation of ethanol to acetaldehyde. In this study, the authors demonstrate how the presence of ceria near the active metal nanoparticles (like we observed in TEM Fig. 3 and S6), significantly increases the dehydroxylation yields of alcohol, due to an oxidative spillover mechanism assisted by the oxidizing properties of the redox couple $\text{Ce}^{+4} \leftrightarrow \text{Ce}^{+3}$. In addition to a possible contribution of the support, the study by Mauri et al. [36] sheds light on the important role that the passivation layers of IMCs have in the methanol decomposition mechanism. Combining experimental and computational studies it has in fact been demonstrated how an oxidized surface favors the processes of alcoholic dehydrogenation compared to the not oxidized Ni-Sn IMCs even under alkaline conditions. The presence of surface oxides in all the catalysts present in this study, demonstrated via XPS (Fig. 8), ^{119}Sn -Mössbauer (Fig. 6), HR-TEM (Figs. S7 and 5) and XAS could therefore potentially promote the dehydrogenation of ethylene glycol to glycol aldehyde by triggering (together with the strong alkaline environment) the formation of GA.

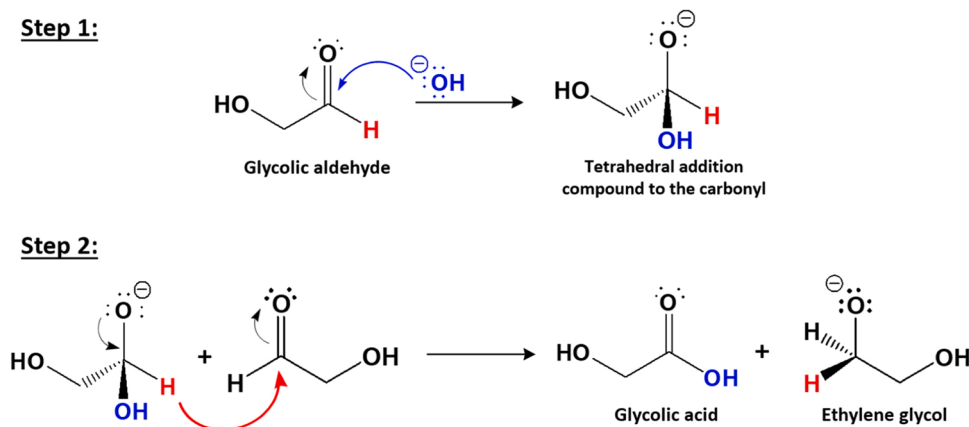
The key mechanism in the formation of glycolic acid, at that point, would be a base-induced disproportionation reaction of the non-enolizable α -hydroxy aldehyde, often referred to as the Cannizzaro reaction [46]. In this reaction, two molecules of glycolic aldehyde, catalyzed by an alkali-induced reaction are converted into a carboxylic acid (glycolic acid) and a primary alcohol (ethylene glycol) as shown in Scheme 2. While a further oxidation of the second alcohol group of the glycolic aldehyde would lead to the formation of glyoxal, which would further be converted to glycolic acid. The true competitive reaction to

that of Cannizzaro, is a probable aldolic condensation which would again lead to the formation of polyalcohols with chains longer than two carbon atoms and C_{3-4+} gaseous products (Scheme 1, Figure S11-B).

The Cannizzaro mechanism proposed as an additional path to the direct aqueous-phase reforming of ethylene glycol is therefore not only capable of explaining the distribution of the products of the liquid phase from the bimetallic catalysts but being an ethylene glycol and H_2 producing mechanism, it also explains the increased conversions and increased hydrogen yields of the catalysts. Furthermore, Pipitone et al. [49] using $\text{Pt}/\text{Al}_2\text{O}_3$ found glycolic acid to be potentially more reactive under APR conditions than ethylene glycol. In addition to its genesis being purely hydrogen-productive, a catalyst active enough to decarboxylate it, could in turn reform the methanol produced as described by path I but with the substantial advantage compared to the canonical path, that a molecule of CO_2 will already be usable for the WGS reaction. This would explain the substantial difference in conversion and selectivity for CO_2 found in the reaction in alkaline environment of monometallic tin catalysts compared to the bimetallic ones. The increased values of conversion in 10Ni-CZ_red under alkaline conditions could mean a competition between the paths I and V in this catalyst (Scheme 1). In fact, it cannot be excluded that the absence of GA in the liquid phase could be derived from its subsequent decarboxylation with the formation of methanol and CO_2 , which, given the intrinsic nature of nickel, would also lead to methanation with a consequent partial consumption of hydrogen and carbon dioxide.

The distribution of the products obtained from the bimetallic catalysts under alkaline conditions (Figs. 12-B, S11-B and 11-B), seem to follow the same conceptual logic as that rationalized for the results obtained under neutral conditions for the same samples. In good agreement with the assumption that the tin-nickel electron transfer generates an increase in the activation energies for some of the cleavage mechanisms and thus weakening the intrinsic activity of nickel.

The tin mitigating effect, already at the lowest concentrations, seems to make the Cannizzaro reaction competitive in alkaline conditions. In comparison with the pathways involving the direct cleavage of ethylene glycol, resulting in an overproduction of glycolic acid. The distribution of metallic and intermetallic species once again proves to be decisive. The 2.510SnNi-CZ_red sample, shown to have Ni nanoparticles with a fine dispersion of a distorted Ni_3Sn (Table S2, Table 2), has the highest feed conversion value among the bimetallic catalysts. Although the hydrogen uptake values derived from H_2 chemisorption show a clear lowering of the accessibility of the nickel present in this sample, the high methanol values found in the liquid phase suggest that the Ni^0 and Ni_3Sn phases may still be potentially active in the further cleavage of the produced glycolic acid towards a methanol decomposition and WGS reaction only, due to the influence of tin in suppressing the methanation



Scheme 2. : Possible Cannizzaro reaction mechanism, proposed as an explanation for the formation of glycolic acid in the APR of ethylene glycol under alkaline conditions.

reaction. The cleavage properties tend to weaken as the concentration of tin in the samples increases (Fig. 12-B), the sample 1010SnNi-CZ_red, contains Ni_3Sn , Ni_3Sn_2 and small quantities of Ni^0 (Fig. 2, Fig. 6), as well as being the least catalytically active, it seems to retain a highly selective reactivity for the Cannizzaro reaction with almost no other products but GA (Scheme 1, Fig. 12-B). Finally, the 510SnNi-CZ_red sample seems to possess an almost optimal distribution of these catalytic properties. The presence of a higher crystalline concentration of Ni_3Sn , combined with the Ni^0 nanoparticles in synergy with an oxidizing support and a pro-active oxidized component, lead to high conversion of EG under alkaline conditions (equal to about 78%) among the bimetallic catalysts. The hydrogen time yield of this catalyst, at 0.86 min^{-1} (calculated based solely on the $\text{Ni}_{\text{wt.}}$ content, Table S5), can be considered aligned with the values reported by Shabaker et al. for the Raney-Ni and Raney Ni_4Sn systems (1.1 and 1.2 min^{-1} respectively [29]) operated at 225°C under neutral conditions and by the $15\%\text{Ni}/\text{CNF}$ (1.34 min^{-1}) reported by van Haastrecht in APR of EG at 230°C in alkaline environment [13]. Although lower hydrogen-yielding compared to the more expensive $5\%\text{Pt}/\text{Al}_2\text{O}_3$ (TOF = 1.6 min^{-1} [50] at 230°C), the catalytic system reported in this work, exhibits remarkably high and tunable selectivity towards glycolic acid in the liquid phase associated with a high EG conversion as a function of tin content. Most catalysts show mass balances exceeding 90% (Table S5). The deficit carbon concentration and its speciation within the liquid and solid phases (spent catalyst) can be partly explained (especially under alkaline conditions) by the partial solubilization of CO_2 into carbonate species [51]. However, it cannot be ruled out that, given the relatively harsh conditions in this experiment, part of this carbonaceous fraction may adhere to the catalyst. Further investigations to detail this specific phenomenon will be conducted in the near future.

4. Conclusions

In this study, three different intermetallic Ni-Sn compounds with different crystallographic arrangements, supported on cerium-zirconium mixed oxides were synthesized by reductive sintering. Their textural, morphological and physico-chemical characteristics were studied throughout the entire synthetic process to correlate the differences to the catalytic results. The ^{119}Sn -Möbbsbauer and XRD analyses, for samples 2.510SnNi-CZ_red and 510SnNi-CZ_red, unraveled a crystallographic arrangement consisting of Ni^0 and the intermetallic Ni_3Sn compound (IMCs), present in a distorted state for 2.510SnNi-CZ_red sample, and of hexagonal geometry and well-defined crystallinity for the 510SnNi-CZ_red sample. On the other hand, the sample with the highest tin content, 1010SnNi-CZ_red, was shown to contain a modest relative abundance of Ni^0 and Ni_3Sn and a conspicuous amount of Ni_3Sn_2 . Thermogravimetric analysis in a reductive environment (TPR-TGA) showed that the catalyst support strongly influences the reduction and sintering process which itself has an effect on the formation of Ni-Sn IMCs. The investigation on the monometallic catalysts containing only tin in the CZ support showed that Sn^{4+} has a strong interaction with the CZ, suppressing the reduction with loading dependency of tin. In the bimetallic catalysts the presence of nickel facilitates the reduction of tin. In the latter, although the reduction takes place completely, it has been demonstrated through XPS, XAS and TEM that exposure of IMCs to an oxygenated environment causes partial passivation, with the formation of an amorphous oxide layer. According to information gathered through analysis of the isomeric shifts of ^{119}Sn nuclei, aided by the analysis of the variation in the density of the occupied states at the Ni K-edge of samples containing IMCs, there appears to be a $\text{Sn} \rightarrow \text{Ni}$ electron density donation capable of diminishing the intrinsic chemisorptive properties of nickel. Analytical studies of the chemisorption properties of bimetallic catalysts in comparison with the 10Ni-CZ_red catalyst used as a reference have shown that the Sn-Ni combination significantly lowers the number of Ni^0 active sites for chemisorption. From the catalytic point of view, the tests carried out under standard conditions

($\text{pH}_i=7$) showed how the “mitigating effect” of the Sn-mediated interaction with Ni^0 constrains the reaction pathways favored over the monometallic nickel catalyst, suppressing the methanation reaction but also limiting the feed conversion as the tin content increases in the IMCs involved. On the other hand, tests conducted under alkaline conditions ($\text{pH}_i=14$) showed a significant increase in EG conversion, increased selectivity for H_2 -producing pathways and thus high hydrogen yields, especially for the 510SnNi-CZ_red catalyst. The reason for the found increased conversion of ethylene glycol together with a higher hydrogen yield under initial alkaline conditions was attributed to the competitive conversion of the feed into glycolic acid via the hydrogen-producing Cannizzaro reaction. The further decarboxylation of glycolic acid with a related production of CO_2 and methanol would allow the continuation of the reforming process via WGS or methanation reactions. The presence of tin in the bimetallic catalysts has therefore been found to be essential in tuning the cleavage properties and the selective suppression of the methane-productive properties found for the monometallic nickel catalyst hence in synergy with the Cannizzaro reaction induced by the alkaline environment, obtaining a positive and tunable combination of effects in terms of conversion and hydrogen selectivity and yield. The high yields of hydrogen combined with the negligible values of methane produced make the metallic and intermetallic arrangement found in the 510SnNi-CZ_red catalyst, a promising starting point for simultaneous production of hydrogen and a fine chemical such as glycolic acid starting from aqueous solution of ethylene glycol at alkaline conditions.

CRediT authorship contribution statement

Sylvio Indris: Validation, Investigation, Formal analysis, Data curation. **Enrico Tusini:** Formal analysis, Data curation. **Monica Pazos Urrea:** Validation, Formal analysis, Data curation. **Margarita Popova:** Validation, Supervision, Resources. **Consolato Rosmini:** Writing – review & editing, Writing – original draft, Visualization, Validation, Software, Investigation, Formal analysis, Data curation, Conceptualization. **Anna Zimina:** Validation, Supervision, Formal analysis. **Hristo Kolev:** Validation, Formal analysis. **Daniela Karashanova:** Validation, Formal analysis. **Daniela Kovacheva:** Validation, Formal analysis. **Jan-Dierk Grunwaldt:** Supervision, Project administration. **Momtchil Dimitrov:** Writing – review & editing, Validation, Supervision. **Magnus Rønning:** Writing – review & editing, Supervision, Project administration.

Declaration of Competing Interest

The authors declare that they have no known competing financial interests or personal relationships that could have appeared to influence the work reported in this paper.

Data availability

Data will be made available on request.

Acknowledgements

This research was funded by the BIKE project, which received funding from the European Union's Horizon 2020 Research and Innovation Program under the Marie Skłodowska-Curie grant agreement no. 813748 and the European Regional Development Fund within the Operational Programme Science and Education for Smart Growth 2014–2020 under the Project Center of Excellence: National center of mechatronics and clean technologies- BG05M2OP001-1.001-0008. The Research Council of Norway is acknowledged for the support to the national infrastructure NorBioLab (project number 270038).

We would like to thank the Institute for Beam Physics and Technology (IBPT) for the operation of the storage ring, the Karlsruhe Research Accelerator (KARA). We acknowledge KIT Light Source for

provision of instruments at the CAT-ACT beamline of the Institute of Catalysis Research and Technology (IKFT). The operation of CAT-ACT beamline is supported by MTET program of Helmholtz Association. Research equipment of Distributed Research Infrastructure INFRAMAT, part of Bulgarian National Roadmap for Research Infrastructures, supported by Bulgarian Ministry of Education and Science was used in this investigation.

Appendix A. Supporting information

Supplementary data associated with this article can be found in the online version at [doi:10.1016/j.apcatb.2024.123904](https://doi.org/10.1016/j.apcatb.2024.123904).

References

- [1] A. Bahadoran, Q. Liu, S. Ramakrishna, B. Sadeghi, M.M. De Castro, P.D. Cavaliere, Hydrogen production as a clean energy carrier through heterojunction semiconductors for environmental remediation, *Energies* 15 (2022) 3222, <https://doi.org/10.3390/en15093222>.
- [2] L. Fan, Z. Tu, S.H. Chan, Recent development of hydrogen and fuel cell technologies: a review, *Energy Rep.* 7 (2021) 8421–8446, <https://doi.org/10.1016/j.egy.2021.08.003>.
- [3] A.B. Leoneti, V. Aragão-Leoneti, S.V.W.B. de Oliveira, Glycerol as a by-product of biodiesel production in Brazil: alternatives for the use of unrefined glycerol, *Renew. Energy* 45 (2012) 138–145, <https://doi.org/10.1016/j.renene.2012.02.032>.
- [4] K. Qi, Z. Li, C. Zhang, X. Tan, C. Wan, X. Liu, L. Wang, D. Lee, Biodegradation of real industrial wastewater containing ethylene glycol by using aerobic granular sludge in a continuous-flow reactor: performance and resistance mechanism, *Biochem. Eng. J.* 161 (2020) 107711, <https://doi.org/10.1016/j.bej.2020.107711>.
- [5] R.D. Cortright, R.R. Davda, J.A. Dumesic, Hydrogen from catalytic reforming of biomass-derived hydrocarbons in liquid water, *Nature* 418 (2002) 964–967, <https://doi.org/10.1038/nature01009>.
- [6] R.R. Davda, J.W. Shabaker, G.W. Huber, R.D. Cortright, J.A. Dumesic, A review of catalytic issues and process conditions for renewable hydrogen and alkanes by aqueous-phase reforming of oxygenated hydrocarbons over supported metal catalysts, *Appl. Catal. : Environ.* 56 (2005) 171–186, <https://doi.org/10.1016/j.apcatb.2004.04.027>.
- [7] T. van Haasterecht, C.C.I. Ludding, K.P. de Jong, J.H. Bitter, Stability and activity of carbon nanofiber-supported catalysts in the aqueous phase reforming of ethylene glycol, *J. Energy Chem.* 22 (2013) 257–269, [https://doi.org/10.1016/S2095-4956\(13\)60032-7](https://doi.org/10.1016/S2095-4956(13)60032-7).
- [8] G. Pipitone, G. Zoppi, R. Pirone, S. Bensaid, A critical review on catalyst design for aqueous phase reforming, *Int. J. Hydrog. Energy* 47 (2022) 151–180, <https://doi.org/10.1016/j.ijhydene.2021.09.206>.
- [9] A. Streb, M. Hefti, M. Gazzani, M. Mazzotti, Novel Adsorption Process for Co-Production of Hydrogen and CO₂ from a Multicomponent Stream, *Ind. Eng. Chem. Res.* 58 (2019) 17489–17506, <https://doi.org/10.1021/acs.iecr.9b02817>.
- [10] S. Sircar, W.C. Kratz, Simultaneous production of hydrogen and carbon dioxide from steam reformer off-gas, *PSA, Sep. Sci. Tech.* 23 (1988) 2397–2415, <https://doi.org/10.1080/01496398808058461>.
- [11] G.W. Huber, J.W. Shabaker, J.A. Dumesic, Raney Ni-Sn catalyst for H₂ production from biomass-derived hydrocarbons, *Science* 300 (2003) 2075–2077, <https://doi.org/10.1126/science.1085597>.
- [12] A.S. Oliveira, J.A. Baeza, D. García, B. Saenz de Miera, L. Calvo, J.J. Rodríguez, M. A. Gilarranz, Effect of basicity in the aqueous phase reforming of brewery wastewater for H₂ production, *Renew. Energy* 148 (2020) 889–896, <https://doi.org/10.1016/j.renene.2019.10.173>.
- [13] T. van Haasterecht, C.C.I. Ludding, K.P. de Jong, J.H. Bitter, Toward stable nickel catalysts for aqueous phase reforming of biomass-derived feedstock under reducing and alkaline conditions, *J. Catal.* 319 (2014) 27–35, <https://doi.org/10.1016/j.jcat.2014.07.014>.
- [14] T. Tsoncheva, C. Rosmini, M. Dimitrov, G. Issa, J. Henych, Z. Němečková, D. Kovacheva, N. Velinov, G. Atanasova, I. Spassova, Formation of catalytic active sites in hydrothermally obtained binary ceria–iron oxides: composition and preparation effects, *ACS Appl. Mater. Interfaces* 13 (2021) 1838–1852, <https://doi.org/10.1021/acsami.0c16326>.
- [15] H.M. Rietveld, Line profiles of neutron powder-diffraction peaks for structure refinement, *Acta Cryst.* 22 (1967) 151–152, <https://doi.org/10.1107/S0365110x67000234>.
- [16] A. Zimina, K. Dardenne, M.A. Denecke, D.E. Doronkin, E. Hüttel, H. Lichtenberg, S. Mangold, T. Pruessmann, J. Rothe, T. Spangenberg, et al., *Rev. Sci. Instrum.* 88 (2017) 113113, <https://doi.org/10.1063/1.4999928>.
- [17] D.C. Koningsberger, R. Prins, *X-ray absorption: principles, applications, techniques of EXAFS, SEXAFS, and XANES*, Wiley, United States, 1988. ISBN: 978-0-471-87547-5.
- [18] B. Ravel, M. Newville, *J. Synchrotron Radiat.* 12 (2005) 537–541, <https://doi.org/10.1107/S0909049505012719>.
- [19] S.I. Zabinsky, J.J. Rehr, A. Ankudinov, R.C. Albers, M.J. Eller, Multiple-scattering calculations of X-ray absorption spectra, *Phys. Rev. B* 52 (1995) 2995–3009, <https://doi.org/10.1103/physrevb.52.2995>.
- [20] C. Klauber, Refinement of magnesium and aluminium K α x-ray source functions, *Surf. Interface Anal.* 20 (1993) 703–715, <https://doi.org/10.1002/sia.740200815>.
- [21] D. Shirley, High-resolution X-ray photoemission spectrum of the valence bands of gold, *Phys. Rev. B* 5 (1972) 4709–4714, <https://doi.org/10.1103/PhysRevB.5.4709>.
- [22] J.H. Scofield, Theoretical photoionization cross sections from 1 to 1500 keV, *J. Electron Spectrosc. Relat. Phenom.* 8 (1976) 129, [https://doi.org/10.1016/0168-1273\(76\)90001-0](https://doi.org/10.1016/0168-1273(76)90001-0).
- [23] F. Moulder, W.F. Sticke, P.E. Sobol, K.D. Bombel, in: *Handbook of X-ray Photoelectron Spectroscopy* (Vol. Second edition), Perkin-Elmer Corporation, Physical Electron Division, Minnesota, USA, 1992. ISBN 0962702625, 9780962702624.
- [24] M. Pazos Urrea, F. Herold, D. Chen, M. Rønning, Nitrogen-containing carbon nanofibers as supports for bimetallic Pt-Mn catalysts in aqueous phase reforming of ethylene glycol, *Catal. Today* 418 (2023) 114066, <https://doi.org/10.1016/j.cattod.2023.114066>.
- [25] T. Matthias, K. Katsumi, N.V. Alexander, O.P. James, R.R. Rouquerol, J.S. Kenneth, Physisorption of gases, with special reference to the evaluation of surface area and pore size distribution (IUPAC Technical Report), *Pure Appl. Chem.* 87 (2015) 1051–1069, <https://doi.org/10.1515/pac-2014-1117>.
- [26] S. Mendioroz, J.A. Pajares, I. Benito, C. Pesquera, F. Gonzalez, C. Blanco, Texture evolution of montmorillonite under progressive acid treatment: change from H₃ to H₂ type of hysteresis, *Langmuir* 3 (1987) 676–681, <https://doi.org/10.1021/la00077a017>.
- [27] A. Onda, T. Komatsu, T. Yashima, Characterizations and catalytic properties of fine particles of Ni-Sn intermetallic compounds supported on SiO₂, *Jour. Catal.* 221 (2004) 378–385, <https://doi.org/10.1016/j.jcat.2003.08.012>.
- [28] S. Indris, M. Schuermann, S.M. Becker, V. Šepelák, R. Kruk, J. Suffer, F. Gyger, C. Feldmann, A.S. Ulrich, H. Hahn, Local structural disorder and relaxation in SnO₂ nanostructures studied by ¹¹⁹Sn MAS NMR and ¹¹⁹Sn Mössbauer spectroscopy, *J. Phys. Chem. C* 115 (2011) 6433–6437, <https://doi.org/10.1021/jp200651m>.
- [29] J.W. Shabaker, G.W. Huber, J.A. Dumesic, Aqueous-phase reforming of oxygenated hydrocarbons over Sn-modified Ni catalysts, *J. Catal.* 222 (2004) 180–191, <https://doi.org/10.1016/j.jcat.2003.10.022>.
- [30] H. Leidheiser, I. Czakó-Nagy, M.L. Varsányi, A. Vértés, Mössbauer spectroscopy of electrodeposited tin-nickel alloys and thermally prepared Ni₃Sn₂, NiSn, and Ni₃Sn₄, *J. Electrochem. Soc.* 126 (1979) 204–208, <https://doi.org/10.1149/1.1212906>.
- [31] R. Mildnerberger, A. Venskutonis, F. Aubertin, J. Brems, G. Schwitzgebel, Electrochemically deposited Ni-Sn alloys: A ¹¹⁹Sn Mössbauer study, *Hyperfine Interact.* 112 (1998) 151–154, <https://doi.org/10.1023/A:1011065400749>.
- [32] J. Silver, C.A. Mackay, J.D. Donaldson, A systematic investigation of the Mössbauer parameters of some intermetallic compounds and electrodeposited alloys of tin, *J. Mater. Sci.* 11 (1976) 836–842, <https://doi.org/10.1007/BF00542298>.
- [33] W.T. Figueiredo, G.B. Della Mea, M. Segala, D.L. Baptista, C. Escudero, V. Pérez-Dieste, F. Bernardi, Understanding the strong metal-support interaction (SMSI) effect in Cu_xNi_{1-x}/CeO₂ (0 < x < 1) nanoparticles for enhanced catalysis, *ACS Appl. Nano Mater.* 2 (2019) 2559–2573, <https://doi.org/10.1021/acsanm.9b00569>.
- [34] Z. Zhang, Z. Yu, K. Feng, B. Yan, Eu³⁺ doping-promoted Ni-CeO₂ interaction for efficient low-temperature CO₂ methanation, *Appl. Catal. B* 317 (2022) 121800, <https://doi.org/10.1016/j.apcatb.2022.121800>.
- [35] C. Rosmini, T. Tsoncheva, D. Kovacheva, N. Velinov, H. Kolev, D. Karashanova, M. Dimitrov, B. Tsyntarski, D. Sebastián, M.J. Lázaro, Mesoporous Ce-Fe-Ni nanocomposites encapsulated in carbon nanofibers: synthesis, characterization and catalytic behavior in oxygen evolution reaction, *Carbon* 196 (2022) 186–202, <https://doi.org/10.1016/j.carbon.2022.04.036>.
- [36] S. Mauri, G. D'Olimpio, C. Ghica, L. Braglia, C.N. Kuo, M. Cosmin Istrate, C.S. Lue, L. Ottaviano, T. Klimczuk, D.W. Boukhvalov, A. Politano, P. Torelli, Hydrogen production mechanism in low-temperature methanol decomposition catalyzed by Ni₃Sn₄ intermetallic compound: a combined operando and density functional theory investigation, *J. Phys. Chem. Lett.* 14 (2023) 1334–1342, <https://doi.org/10.1021/acs.jpclett.2c03471>.
- [37] H. Knozinger, F. Schuth, J. Weitkamp, in: *Handbook of Heterogeneous Catalysis*, second ed., Wiley-VCH Verlag GmbH & Co, KGaA, Weinheim, 2008. Copyright ©.
- [38] B. Hammer, J. Norskov, Why gold is the noblest of all the metals, *Nature* 376 (1995) 238–240, <https://doi.org/10.1038/376238a0>.
- [39] K. Balakrishnan, J. Schwank, A chemisorption and XPS study of bimetallic Pt-Sn/Al₂O₃ catalysts, *Jour. Catal.* 127 (1991) 287–306, [https://doi.org/10.1016/0021-9517\(91\)90227-U](https://doi.org/10.1016/0021-9517(91)90227-U).
- [40] S. Penner, M. Armbrüster, Formation of intermetallic compounds by reactive metal-support interaction: a frequently encountered phenomenon in catalysis, *Chemcatchem* 7 (2015) 374–392, <https://doi.org/10.1002/cctc.201402635>.
- [41] J.W. Shabaker, G.W. Huber, R. Cortright, Kinetics of aqueous-phase reforming of oxygenated hydrocarbons: Pt/Al₂O₃ and Sn-modified Ni catalysts, *Ind. Eng. Chem. Res.* 43 (2004) 3105, <https://doi.org/10.1021/e049852o>.
- [42] T. Tsoncheva, C. Rosmini, M. Mihaylov, J. Henych, K. Chakarova, N. Velinov, D. Kovacheva, Z. Němečková, M. Kormunda, R. Ivanova, I. Spassova, K. Hadjiivanov, Nickel-decorated mesoporous iron–cerium mixed oxides: microstructure and catalytic activity in methanol decomposition, *ACS Appl. Mater. Interfaces* 14 (2022) 873–890, <https://doi.org/10.1021/acsami.1c19584>.
- [43] J.W. Shabaker, D.A. Simonetti, R.D. Cortright, J.A. Dumesic, Sn-modified Ni catalysts for aqueous-phase reforming: characterization and deactivation studies, *J. Catal.* 231 (2005) 67–76, <https://doi.org/10.1016/j.jcat.2005.01.019>.
- [44] Y. Xu, H. Jin, T. Hirano, Y. Matsushita, J. Zhang, Characterization of Ni₃Sn intermetallic nanoparticles fabricated by thermal plasma process and catalytic

- properties for methanol decomposition, *Sci. Technol. Adv. Mater.* 17 (2019) 622–631, <https://doi.org/10.1080/14686996.2019.1622447>.
- [45] Y. Wang, Bioadaptability: an innovative concept for biomaterials, *J. Mater. Sci. Technol.* 32 (2016) 801–809, <https://doi.org/10.1016/j.jmst.2016.08.002>.
- [46] Y. Zhan, W. Hou, G. Li, Y. Shen, Y. Zhang, Y. Tang, Oxidant-free transformation of ethylene glycol toward glycolic acid in water, *ACS Sustain. Chem. Eng.* 7 (2019) 17559–17564, <https://doi.org/10.1021/acssuschemeng.9b04617>.
- [47] V.V. Torbina, A.A. Vodyankin, S. Ten, G.V. Mamontov, M.A. Salaev, V.I. Sobolev, O.V. Vodyankina, Ag-based catalysts in heterogeneous selective oxidation of alcohols: a review, *Catalysts* 8 (2018) 447, <https://doi.org/10.3390/catal8100447>.
- [48] M.V. Grabchenko, G.V. Mamontov, V.I. Zaikovskii, Effect of the metal–support interaction in Ag/CeO₂ catalysts on their activity in ethanol oxidation, *Kinet. Catal.* 58 (2017) 642–648, <https://doi.org/10.1134/S0023158417050056>.
- [49] G. Pipitone, G. Zoppi, S. Ansaloni, S. Bocchini, F.A. Deorsola, R. Pirone, S. Bensaid, Towards the sustainable hydrogen production by catalytic conversion of C-laden biorefinery aqueous streams, *Chem. Eng. J.* 377 (2019) 120677, <https://doi.org/10.1016/j.cej.2018.12.137>.
- [50] T. van Haasterecht, C.C.I. Ludding, K.P. de Jong, J.H. Bitter, Stability and activity of carbon nanofiber-supported catalysts in the aqueous phase reforming of ethylene glycol, *J. Energy Chem.* 22 (2013) 257–269, [https://doi.org/10.1016/S2095-4956\(13\)60032-7](https://doi.org/10.1016/S2095-4956(13)60032-7).
- [51] J. Liu, X. Chu, L. Zhu, J. Hu, R. Dai, S. Xie, Y. Pei, S. Yan, M. Qiao, K. Fan, Simultaneous aqueous-phase reforming and KOH carbonation to produce CO_x-free hydrogen in a single reactor, *ChemSusChem* 3 (2010) 803–806, <https://doi.org/10.1002/cssc.201000093>.